Prototype of a Warn-on-Forecast System for Smoke (WoFS-Smoke)

THOMAS JONES,[a,b,c] RAVAN AHMADOV,[d,e] ERIC JAMES,[d,e] GABRIEL PEREIRA,[f] SAULO FREITAS,[g] AND GEORG GRELL[e]

[a] *Cooperative Institute for Severe and High-Impact Weather Research and Operations, University of Oklahoma, Norman, Oklahoma*
[b] *NOAA/National Severe Storms Laboratory, Norman, Oklahoma*
[c] *School of Meteorology, University of Oklahoma, Norman, Oklahoma*
[d] *Cooperative Institute for Research in Environmental Sciences, University of Colorado, Boulder, Colorado*
[e] *NOAA/OAR/Global Systems Laboratory, Boulder, Colorado*
[f] *Federal University of São João del-Rei, São João del-Rei, Brazil*
[g] *USRA/GESTAR and NASA Goddard Space Flight Center, Greenbelt, Maryland*

(Manuscript received 30 August 2021, in final form 20 April 2022)

ABSTRACT: This research begins the process of creating an ensemble-based forecast system for smoke aerosols generated from wildfires using a modified version of the National Severe Storms Laboratory (NSSL) Warn-on-Forecast System (WoFS). The existing WoFS has proven effective in generating short-term (0–3 h) probabilistic forecasts of high-impact weather events such as storm rotation, hail, severe winds, and heavy rainfall. However, it does not include any information on large smoke plumes generated from wildfires that impact air quality and the surrounding environment. The prototype WoFS-Smoke system is based on the deterministic High-Resolution Rapid Refresh-Smoke (HRRR-Smoke) model. HRRR-Smoke runs over a continental United States (CONUS) domain with a 3-km horizontal grid spacing, with hourly forecasts out to 48 h. The smoke plume injection algorithm in HRRR-Smoke is integrated into the WoFS forming WOFS-Smoke so that the advantages of the rapidly cycling, ensemble-based WoFS can be used to generate short-term (0–3 h) probabilistic forecasts of smoke. WoFS-Smoke forecasts from three wildfire cases during 2020 show that the system generates a realistic representation of wildfire smoke when compared against satellite observations. Comparison of smoke forecasts with radar data show that forecast smoke reaches higher levels than radar-detected debris, but exceptions to this are noted. The radiative effect of smoke on surface temperature forecasts is evident, which reduces forecast errors compared to experiments that do not include smoke.

KEYWORDS: Numerical weather prediction/forecasting; Short-range prediction; Wildfires

1. Introduction

During the summer and fall of 2020, dozens of lives were lost in association with wildfires occurring in the western United States. These fires also destroyed thousands of homes and businesses while burning millions of acres of land. These fires also led to record low air quality levels being recorded over much of this region. Lofted debris, ash, and smoke from intense wildfires can reach well into the mid and upper troposphere (e.g., Lareau et al. 2018) and smoke aerosols may persist in the atmosphere for many days before deposition occurs or they break down chemically (e.g., Pope et al. 2002). Pyrocumulus (pyroCu) and pyro-cumulonimbus (pyroCb) can be formed by buoyant updrafts generated by the extreme heat, evaporated moisture from burning biomass, and smoke aerosols acting as cloud condensation nuclei (e.g., Potter 2012; Lindsey et al. 2010; Peterson et al. 2015, 2017; Fromm et al. 2006, 2010, 2016). Furthermore, smoke and debris in the atmosphere downstream of the fire can block solar radiation reaching the surface reducing temperature. (Robock 1988; 1991). These changes to the atmospheric state can even combine to enable the development of severe weather, lightning, and brief tornadoes (e.g., Reader et al. 2009; Coen et al. 2013; Peace et al. 2015; Lareau and Clements 2016; McRae et al. 2013). The rapidly evolving nature of wildfires is one of many reasons that makes forecasting these conditions difficult, but recent advances in wildfire observations and numerical weather prediction (NWP) models have begun to make progress in this endeavor.

The tracking of smoke and its effect on the surrounding environment represents an important area of research in both global and convection allowing NWP systems. Convection allowing models (CAMs) generally focus on resolving and forecasting specific convective features. Accurate short-term (0–3 h) forecasting of smoke produced by individual wildfires and its impact on the environment requires a system with similar capabilities. Smoke associated with these fires varies on the same spatial and temporal scales as those for convection. Only CAMs are run at the grid spacing (<3 km) required to resolve the many smoke–atmosphere interactions that occur. One example of a CAM that meets these requirements is the High-Resolution Rapid Refresh with smoke (HRRR-Smoke; https://rapidrefresh.noaa.gov/hrrr/HRRRsmoke/). This system generates 0–48-h forecasts of smoke aerosol concentrations produced by wildfires using an hourly cycling data assimilation system with a 3-km grid spacing (Benjamin et al. 2016). Smoke aerosols are defined as the particulate mass of particles smaller than 2.5 μm in median diameter (PM2.5). HRRR-Smoke ingests fire radiative power (FRP) information from

Corresponding author: Thomas A. Jones, Thomas.Jones@noaa.gov

DOI: 10.1175/WAF-D-21-0143.1

polar orbiting satellite sensors such as Moderate Resolution Imaging Spectroradiometer (MODIS) and Visible Infrared Imaging Radiometer Suite (VIIRS) initiate smoke aerosols within the model (Freitas et al. 2007; Ahmadov et al. 2017). Smoke aerosols are allowed to evolve during the forecast period with feedback between the model radiation scheme and the smoke aerosols is allowed. However, full coupling with cloud microphysics schemes has not yet been implemented in this system (e.g., Grell et al. 2005; Thompson and Eidhammer 2014). HRRR-Smoke has recently (late 2020) been declared operational as part of HRRRv4, and deterministic forecasts of 3D smoke aerosol concentrations along with surface visibility are currently being generated.

HRRR-Smoke is a deterministic forecast system and little research into short-term probabilistic forecasts of these phenomena using ensemble-based NWP techniques has occurred. A deterministic system such as HRRR-Smoke only has the ability to generate a single forecast from a particular initialization time; thus, it has a limited ability to account for the many potential uncertainties in both the observations and the model itself. One solution to this issue to generate probabilistic forecasts from an ensemble so that the forecast spread can be visualized. This work adapts the National Severe Storms Laboratory (NSSL) Warn-on-Forecast System (WoFS) to generate probabilistic forecasts of smoke aerosol concentrations forming a system hereafter defined as WoFS-Smoke. The WoFS is a rapid cycling ensemble data assimilation and forecasting system that runs daily over a region centered around an area of expected high impact weather (Stensrud et al. 2009, 2013; Wheatley et al. 2015; Jones et al. 2016). The WoFS assimilates conventional, radar, and satellite data within a given domain at 15-min intervals to continually update the model analysis to account for a rapidly evolving environment. This system has proven successful in generating skillful short-term (0–3 h) probabilistic forecasts of high impact weather in a real-time forecasting environment (Skinner et al. 2018; Yussouf and Knopfmeier 2019). Similar successes should be attainable with short term forecasts of smoke aerosol content and corresponding atmospheric impacts.

The prototype WoFS-Smoke is based on the WoFS used during real-time test bed activities in 2020 and 2021, but with several modifications to enable a smoke forecasting ability. First, the full HRRR-Smoke smoke aerosol tracking functionality is added to WoFS, which includes the 3D prognostic smoke aerosol mixing ratio variable. Second, smoke aerosol analyses from archived HRRR-Smoke runs for each case are used to initialize the WoFS initial conditions. Third, FRP retrievals are ingested at hourly intervals in WoFS-Smoke to initialize and update smoke aerosols during the cycling period. Finally, probabilistic forecast products of smoke aerosol concentrations are developed for display and verification. The goal is to determine if the WoFS-Smoke can generate realistic forecasts of smoke from qualitative comparisons with satellite and radar observations and quantitative comparisons with surface temperature observations. This is accomplished by testing the system on 3 wildfire cases occurring over the western United States during the summer and fall of 2020. Cases from Arizona (AZ), California (CA), and Colorado (CO) are utilized to provide some geographic diversity when assessing forecast characteristics (Fig. 1). While all of these cases are multiday events, this research will primarily focus on shorter term characteristics during a single afternoon.

Following the introduction, section 2 describes satellite and radar observations of smoke and debris generated from wildfires. Section 3 describes the prototype WoFS-Smoke system and the required changes to transform WoFS into WoFS-Smoke. Model output is compared with satellite and radar observations in section 4 for each wildfire case and finally conclusions follow in section 5.

2. Observations

a. Satellite

Both individual wildfires and the aerosols they inject into the atmosphere are detectable from polar orbiting and geostationary weather satellites. Smoke aerosols lofted into the atmosphere absorb and scatter solar and thermal radiation, and are detectable from satellites using visible and infrared bands (e.g., Coakley et al. 1983; Kaufman et al. 1997; Remer et al. 2005; Liu et al. 2003). Smoke aerosols are often present in the vicinity of clouds and pyroCu and retrieving accurate aerosol characteristics in these conditions is very difficult (e.g., Zhang et al. 2005; Koren et al. 2007).

Wildfires generate intense subpixel heat anomalies which are detectable as elevated brightness temperatures from the shortwave 3.9-μm channel (Dozier 1981; Weaver et al. 1995, 2004). Automated detection algorithms have been developed which use this channel along with visible (0.64 μm) and infrared longwave (11.2 μm) channels to generate a product often labeled as "hotspot" detections (Prins and Menzel 1992, 1994; Prins et al. 1998; Csiszar et al. 2014; Giglio et al. 2016, 2018). These algorithms use statistical methods to determine the location of "hot" pixels and then screen these pixels to remove potential false or misleading detections. Retrieved products may include FRP, fire size (FS), and fire temperature (FT). For polar orbiting sensors, the horizontal resolution can be less than 1 km, but with a low temporal frequency. Retrievals using the Advanced Baseline Imager (ABI) on board the Geostationary Operational Environmental Satellite Series-R (GOES)-R satellites are generated at a 2-km horizontal resolution at 5-min intervals, enabling the rapid evolution of fast moving fires to be measured. FRP can be directly related to the amount of burned material, which in turn is related to the amount of PM2.5 injected into the atmosphere (Kaufman et al. 1998a,b; Wooster et al. 2005; Roberts et al. 2005). These products are used to initialize wildfires and smoke into HRRR-Smoke using the methods described in the following section.

The challenges of wildfire detection from satellites are evident from the hotspot retrievals for each of these cases (Fig. 1). For the period between 1500 and 0100 UTC, all retrievals from the *Suomi National Polar-Orbiting Partnership* (*SNPP*), *NOAA-20*, *Aqua*, *Terra*, and GOES satellites are plotted along with the total FRP from each retrieval for 5-min intervals. For the Bush fire in AZ, the crescent shape of the fire at this time can be seen from all satellites with *GOES-17*

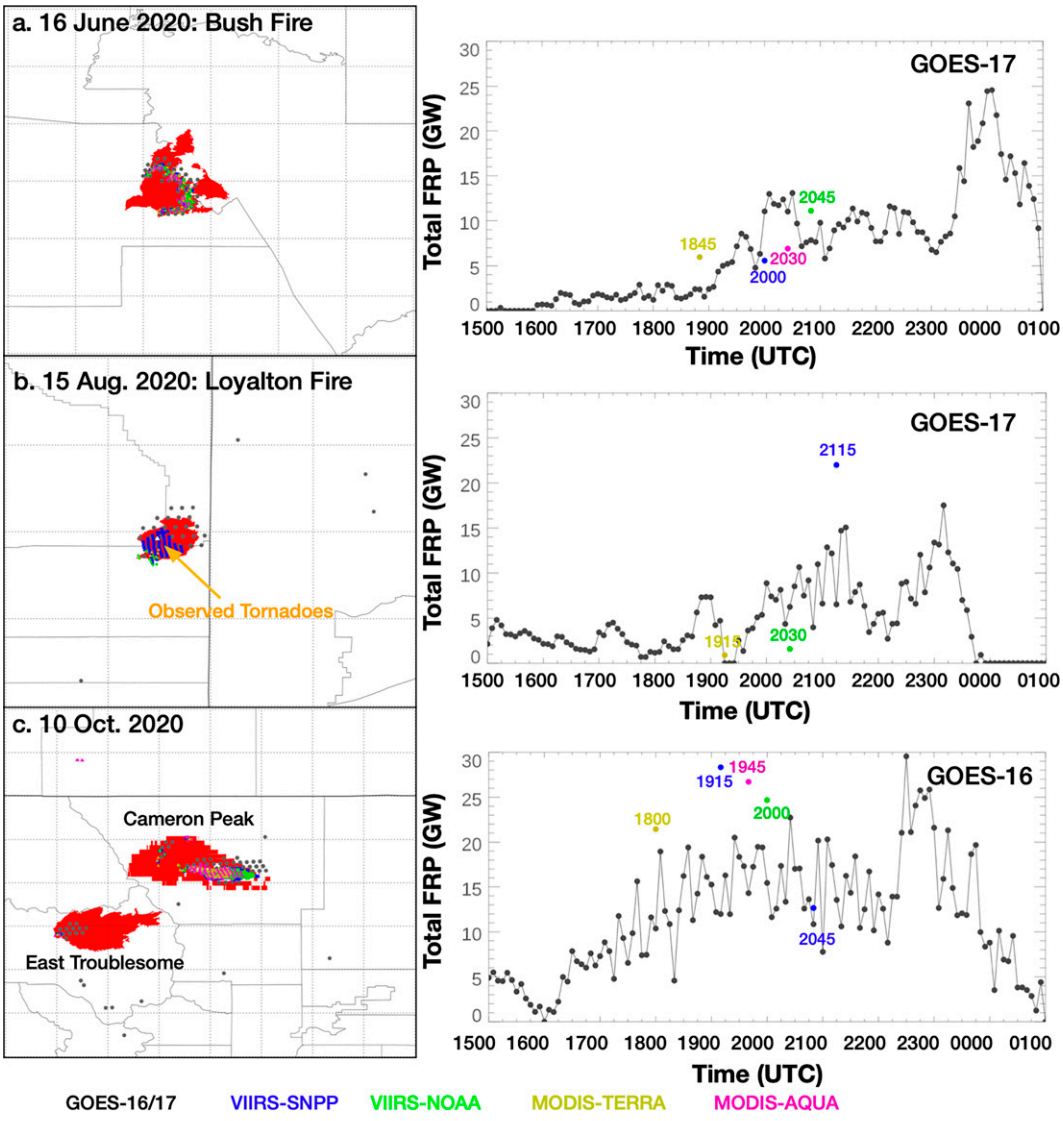

FIG. 1. (left) Fire perimeters associated with the three wildfire days being studied in this research (https://www.nifc.gov). Ongoing fires during these periods are labeled and shaded in red. Overlaid are hotspot retrievals between 1500 and 0100 UTC from the *Terra*, *Aqua*, *SNPP*, *NOAA-20*, and GOES satellites. GOES retrievals are plotted at their native resolution of 2 km, with data from the other sensors having a finer resolution. (right) The sum of FRP for all retrievals within a 5-min window from each satellite in this domain over the same time period.

retrievals indicating an increase in fire intensity after 1900 UTC and a second, larger, increase after 2330 UTC. (Fig. 1a). The total FRP aggregated and number of retrievals from *GOES-17* over the entire 1500–0100 period are provided in Table 1. The higher spatial resolution (<1 km) of the VIIRS and MODIS retrievals is also apparent showing fine details of the overall wildfire structure. However, retrievals from VIIRS and MODIS instruments on board the polar-orbiting satellites are confined to the overpass times between 1845 and 2045 UTC, with no temporal trends being evident. The current (2021) version of HRRR-Smoke as well as the prototype WoFS-Smoke described here only utilize the VIIRS and MODIS retrievals, limiting the potential short-term forecast skill of smoke when wildfires initiate well before or after these overpasses.

In the case of the Loyalton fire in CA, temporal trends in fire intensity are also evident (Fig. 1b). Retrievals from the MODIS

TABLE 1. Total number of *GOES-16* or *GOES-17* FRP retrievals between 1500 and 0100 UTC for each case along with the aggregated FRP over this time period.

Case	Satellite	No.	Total FRP ($\times 10^6$ GW)
16 Jun 2020	*GOES-17*	1580	1.40
15 Aug 2020	*GOES-17*	585	0.55
10 Oct 2020	*GOES-16*	2280	0.83

instrument on board the *Terra* satellite and VIIRS on board the *Aqua* satellite are only present at the extreme southwest edge of the fire near the origin at 1915 and 2030 UTC, but the intensity increases substantially by 2115 UTC during the *SNPP* overpass (Fig. 1b). Corresponding *GOES-17* data indicates an overall increase in fire coverage up to 2300 UTC before rapidly decreasing thereafter. The time series of *GOES-17* retrievals also shows several dips in FRP values, which are likely due to pyroCu obscuring portions of the fire during these periods. Clouds could also be blocking the some of the MODIS and VIIRS retrievals at 1915 and 2030 UTC. Overall, the aggregate FRP and number of retrievals for this case is substantially smaller compared to the Bush fire, with the exception of the *SNPP* retrievals at 2115 UTC (Table 1). Two separate fires are ongoing on 14 October with the largest being the existing Cameron Peak fire and the rapidly developing East Troublesome fire to the southwest (Fig. 1c). For the Cameron Peak fire, *GOES-16*, VIIRS, and MODIS retrievals are generally collocated, though a few VIIRS and MODIS retrievals are present in the East Troublesome fire (Fig. 1c). VIIRS retrievals from the *SNPP* satellite are present at both 1915 and 2045 UTC, which is a result of the fire being on the edge of two consecutive overpasses. *GOES-16* retrievals indicate an increase in fire intensity between 1500 and 1900 UTC. The jump after 2200 UTC is due to the inclusion of those from the East Troublesome fire. This case generated the largest number of retrievals, but the overall aggregated FRP is not as great as observed for the Bush fire (Table 1). The strengths and weaknesses of retrievals from polar orbiting versus geostationary satellites are evident in each case, and will have important implications to the WoFS-Smoke forecasts described in section 4.

b. Weather radar

Ash and debris lofted into the atmosphere from wildfires are also detectable from weather radars such as the WSR-88D Doppler radar (e.g., Banta et al. 1992; Melnikov et al. 2009; Jones and Christopher 2009, 2010a,b; Zrnić et al. 2020). Ash, leaves, pine needles, grass, and man-made objects can all be lofted deep into the atmosphere by buoyant updrafts produced by intense wildfires along with the large amounts of smoke aerosols they generate. Debris are often large enough (diameter $> 100\ \mu$m) to be detectable from precipitation radars whereas smoke aerosols themselves are not (diameter $\sim 1\ \mu$m). Several studies have analyzed the characteristics of debris plumes from radars (including polarimetric radars) and have determined they generate unique characteristics when compared to sampling precipitation (Melnikov et al. 2009; Jones et al. 2009; Zrnić et al. 2020). It has been found that ash and debris are highly nonspherical in nature, unlike raindrops; thus, return low correlation coefficient (RhoHV) values (RhoHV < 0.5). Positive differential reflectivity (ZDR) is also usually observed, indicating that much of the ash and debris is horizontally oriented though vertically oriented debris (ZDR < 0) have been noted within strong updrafts. Ash and debris have been observed being injected into the atmosphere in excess of 10 km above the surface and more than 100 km downstream of the fire (e.g., Jones and Christopher 2009, 2010a,b; Lareau et al. 2018). Given that smoke particles are both smaller and lighter, the radar measurements of debris likely represent a lower bound for the coverage of smoke. While it is important to emphasize the smoke and debris are very different objects, their collocation allows radar data to provide information not possible from passive satellite sensors such as ABI, VIIRS, and MODIS. The radar observations provide high spatial and temporal resolution of the vertical profile of debris concentration that can be directly related to smoke concentrations. This vertical information can then be used as verification for NWP models and eventually as inputs to improve the 3D analysis of smoke within the model.

For this work, reflectivity, ZDR, and RhoHV from individual radars are combined into a 3D gridded product using the Warning Decision Support System–Integrated Information (WDSS-II) software (Lakshmanan et al. 2007). This product is known as Multi-Radar Multi-Sensor (MRMS) product and is generated in real time. Two sets of MRMS data are created for this work. The first mimics the operational configuration while the second turns off several quality control algorithms designed to remove nonprecipitation returns from the data. Data created using the operational configuration are used to generate the reflectivity and radial velocity observations needed for assimilation. Currently, no radar data associated with the wildfires are assimilated into the system. The existing radar forward operators are unable to translate nonprecipitation radar returns into the appropriate model variables. The less quality controlled MRMS products that retain ash and debris information are only used for verification of modeled smoke injection heights and coverage.

3. WoFS-Smoke design

a. Baseline configuration

The WoFS is an ensemble-based data assimilation and forecasting system designed to generate frequent probabilistic forecasts of high impact weather events (Wheatley et al. 2015; Jones et al. 2016, Skinner et al. 2018; Yussouf and Knopfmeier 2019). The 2020–21 configuration of the system utilizes a regional domain approximately 900 km $\times$ 900 km in size centered around the area where high impact weather is expected for a particular day. The system is initialized in the midmorning from analyses and forecasts provided by 36-member HRRR ensemble system currently operated by the Global Systems Laboratory (GSL; Alexander et al. 2018). WoFS contains 36 ensemble members and is initialized at 1500 UTC using 1-h HRRR ensemble forecasts from 1400 UTC. Hourly boundary conditions are provided by 24-h HRRR ensemble forecasts initialized at 1200 UTC. Horizontal grid spacing for both HRRR and the WoFS is 3 km with 51 vertical levels and a model top of ~20 hPa.

Available data are assimilated at 15-min intervals for the duration of each case using the ensemble Kalman filter (EnKF) approach combined with the Community Gridpoint Statistical Interpolation (GSI) software, which contains the necessary forward operators (Whitaker et al. 2008; Kleist et al. 2009;

Hu et al. 2016). The WoFS uses the Advanced Weather Research and Forecasting model (WRF-ARW) version 3.9.1, similar to the version used by GSL for the HRRR ensemble (Skamarock et al. 2008; Powers et al. 2017). The system can assimilate conventional, radar reflectivity, radial velocity, GOES-R cloud water path (CWP), and/or GOES-R all-sky water vapor channel radiances (Wheatley et al. 2015; Jones et al. 2016, 2020). Some observation types may not be assimilated in practice due to data availability and/or relevance to case-specific atmospheric conditions. Ensemble spread is maintained by applying different sets of model boundary layer physics and radiation schemes to each member (Stensrud et al. 2000; Wheatley et al. 2015; Skinner et al. 2018) and adding prior adaptive inflation during each update cycle (Anderson 2009). An outlier threshold of 3.25 standard deviations from the mean is applied to all observation types. Observation localization uses the Gaspari and Cohn (1999) technique with different localization radii being applied for each observation type. See Table 1 in Jones et al. (2020) for specific values.

b. *Changes required for WoFS-Smoke*

Several changes to the baseline WoFS configuration are required to create WoFS-Smoke. HRRR-Smoke uses a subset of the WRF-Chem model (Skamarock et al. 2008; Grell et al. 2005) tuned for smoke aerosol tracking while other aerosol types are not considered. Smoke aerosols are assumed to be generated solely from wildfires and no chemical interactions are included. The smoke tracking component of HRRR-Smoke is added to WoFS-Smoke and activated for these experiments. To initialize each ensemble member, the smoke from the 1500 UTC HRRR-Smoke analysis file is interpolated to the WoFS grid. To foster model spread for smoke in the initial conditions, noise based on a random Gaussian distribution of ±10% is applied. At hourly intervals during the cycling period, FRP data from MODIS and VIIRS are integrated into the analysis using the technique developed for HRRR-Smoke. In summary, raw FRP retrievals from the VIIRS instrument on board the *SNPP* and *NOAA-20* satellites and the MODIS instrument on board the *Terra* and *Aqua* satellites are mapped onto the 3-km HRRR grid with simulated biomass burning emissions calculated at each grid point using parameterization schemes developed by Freitas et al. (2007). Legacy hotspots from previous retrievals are retained for 24 h, with fire intensity set to decrease as a function of age. If a new retrieval occurs at same the location of an existing retrieval, the new data overwrites the previous data and the age is set back to zero. If no valid retrievals exist within a 3-km grid point due to either no fire being present or clouds masking the fire, then plume rise scheme is not applied. Mapping the retrievals to a 3-km grid also means that small, but intense fires observed in the raw VIIRS and MODIS data may be underestimated in the observations used by the model. Plume rise is estimated using a 1D entrainment plume parameterization scheme that ingests model data (temperature, moisture, horizontal and vertical velocity, cloud hydrometeor variables, and land surface conditions) at each model grid point. Using the land surface conditions, fires at each grid point are classified as either forest, woody savanna, or grassland types. Land surface classifications are used to adjust FRP satellite retrievals to estimate convective energy flux (CEF). CEF is then used to calculate parcel buoyancy flux (BF) using Eq. (1), where g = acceleration due to gravity, p_e = ambient surface pressure, C_p = specific heat at a constant pressure, R = ideal gas constant, and r = plume radius calculated from the retrieved FS (Viegas 1998):

$$\mathrm{BF} = \frac{gR}{C_p p_e}\,\mathrm{CEF} r^2. \tag{1}$$

An estimate of vertical velocity is calculated, using BF while accounting for additional latent heat release from condensed moisture and entrainment of the preexisting environment into the buoyant parcel. The maximum injection height is set to the model level in which the vertical velocity of this parcel decreases to less than 1 m s^{-1}. Injection height parameters are transferred back to the NWP model (e.g., WRF), which uses this information to release aerosols into the model analysis. Injection height uncertainties are generally less than ±1 km for a particular grid point (Freitas et al. 2006, 2007). For wildfires that have large gridpoint to gridpoint variations in size and intensity, multiple injection heights may be associated with an individual fire resulting in a complex vertical distribution of aerosols at the analysis time. After being released, aerosols are allowed to interact with the surrounding atmosphere once a forecast has started. As forecast time increases, aerosols continue to disperse as they advect farther from the source region and can fall out of the atmosphere entirely. This system assumes that the buoyant updraft calculated within the 1D plume rise scheme does not directly modify the atmospheric conditions in WRF. While this was found to be an adequate assumption for low-resolution models, it may not be completely adequate for convection allowing models.

This method has proven effective in providing skillful HRRR-Smoke forecasts, but several uncertainties are present. For example, uncertainties in the FRP retrievals, injection height assumptions, and the overall atmospheric conditions cannot be assessed. Since WoFS-Smoke is an ensemble, it is possible to integrate these uncertainties into the system to determine their overall impact to the forecast. A random 30% uncertainty value is applied to the FRP retrievals ingested into each ensemble member. This has the effect of allowing for different smoke injection heights and amounts from member to member while keeping overall values within the realm of realistic expectations.

For this proof-of-concept configuration, smoke is set to zero in the boundary conditions. Future versions will derive this information from operational HRRR-Smoke forecasts. At the bottom of each hour during the assimilation cycling, updated hotspot detections from VIIRS and MODIS data are added so that fires developing after the system's initialization are taken into account. A smoke variable is added to the set of prognostic variables updated by the EnKF so that assimilated data can update the characteristics of smoke without relying on new hotspot information. For this configuration, the

addition of smoke in the EnKF system does not make a large difference since no observations highly correlated with smoke, such as aerosol optical depth (AOD), are assimilated. However, once these data are assimilated to the system, updates to smoke during the cycling process will become much more important.

All ensemble members of WoFS-Smoke use a modified version of the NSSL 2-moment scheme (Ziegler 1985; Mansell et al. 2010) that includes the variables present in the Thompson aerosol aware cloud microphysics schemes (Thompson and Eidhammer 2014). These variables include ice nucleating, nonhygroscopic dust number concentration and hygroscopic cloud droplet concentration from black carbon and sulfate aerosols, which are used by both the cloud microphysics and radiation schemes. Their values are set using monthly climatological averages of aerosol concentrations from the Goddard Chemistry Aerosol Radiation and Transport (GOCART) model (Ginoux et al. 2001) and are not directly linked to the wildfire smoke. However, smoke is directly linked to the Rapid Radiative Transfer Model for General Circulation Models (RRTMG) radiation scheme with thicker smoke plumes resulting in less solar radiation reaching the surface leading to secondary impacts to the surrounding environment. To fully enable this effect in WoFS-Smoke, the RRTMG scheme (also used by the HRRR) is used for all ensemble members. WoFS-Smoke retains the multiple planetary boundary layer (PBL) scheme configuration that uses either the Yonsei University (YSU), Mellor–Yamada–Janjic (MYJ), or the Mellor–Yamada–Nakanishi–Niino (MYNN; Hong et al. 2006; Janjić 1994; Nakanishi and Niino 2006) schemes for one-third of all members.

Only conventional, radar reflectivity, and radial velocity observations are assimilated in the experiments conducted for this research. See Wheatley et al. (2015) and Skinner et al. (2018) for more details on the radar observation processing characteristics. As stated previously, radar data associated with lofted debris are not assimilated. One small change from the baseline system is that velocity data are processed at a higher grid spacing (3 versus 5 km) (Kerr et al. 2021). No satellite observations are assimilated in these experiments, but the capability to assimilate these data remains in place.

Three wildfire cases occurring in the summer and fall of 2020 are selected to evaluate the performance and capabilities of WoFS-Smoke. WoFS-Smoke is initialized at 1500 UTC for all cases and continuously cycled until 0100 UTC. The 0–3-h forecasts for the first 18 ensemble members are initiated at 1900 UTC and at hourly intervals thereafter. Ensemble mean and probabilistic forecasts of smoke aerosol concentrations are then calculated for evaluation. For the 14 October case, the smoke plume covers an area that includes several Automated Surface Observing System (ASOS) sites. A second set of forecasts are generated that do not include smoke to allow for a quantitative assessment of the radiative impacts of smoke on the surface environment.

4. Examples

a. 16 June 2020: Bush fire

On 16 June 2020, several large wildfires were ongoing in AZ with the largest located northeast of Phoenix, known as the Bush fire (Fig. 1a; https://www.nifc.gov/). This fire originated on 13 June in the Tonto National Forecast and spread rapidly through tall grasses in the dry conditions. Nearly 200 000 acres were burned before the fire was under control. Another large wildfire was ongoing in northwestern AZ in the Kaibab National Forest, known as the Mangum fire, that began on June 8 and burned over 70 000 acres of land. The environmental flow carried large amounts of smoke and debris from the fires' origin downstream in a northeasterly direction. Visible (0.47 μm) *GOES-17* imagery at 2200 UTC shows the smoke plumes associated with both major fires and their corresponding hotspot detections at this time (Fig. 2a). The amount of smoke and its distance from the fire increases at later times as shown in the 2330 and 0100 UTC images (Figs. 2b,c). Smoke from the Mangum fire also drifts southeastward due to changes in the midtropospheric wind direction and eventually mixes with the plume from the Bush fire by 0100 UTC.

Maximum column MRMS radar reflectivity associated with debris lofted into the atmosphere by each fire are calculated for comparison with the satellite observations (Figs. 2d–f). Precipitation returns have been filtered out for the most part using the polarimetric variables though some ground clutter does remain. Both fires are evident at 2200 UTC with debris plumes extending northeast from their origin in excess of 100 km in the case of the Bush fire (Fig. 2d). The overall debris plume characteristics do not change much over the following 3 h except that reflectivity associated with the Bush fire increases somewhat by 0100 UTC (Fig. 2f). The location and orientation of the debris plumes is consistent with the satellite observations except that the debris plume is not detectable as far downstream, as expected. Corresponding debris heights derived from radar data show all fires loft debris over 5 km above sea level (>3 km above the surface), with heights slowly decreasing as a function of distance from the fire origin (Figs. 2g–i). Debris height from MRMS data is defined as the highest level where reflectivity is greater than -5 dBZ at a particular location.

To assess the potential of the WoFS-Smoke at analyzing and forecasting smoke generated from these fires, a 3-h WoFS-Smoke forecast initiated at 2200 UTC is analyzed. Hotspot retrievals from VIIRS and MODIS instruments have been ingested into the system at 1900, 2000, and 2100 UTC, so forecasts initiated at 2200 UTC should contain large amounts of smoke. Figure 3 shows 0-, 90-, and 180-min (0, 1.5, 3 h) forecasts of ensemble mean total column smoke along with the corresponding maximum forecast aerosol height, defined as the highest model layer where smoke > 0.1 mg kg^{-1}. Large smoke plumes generated from several fires are clearly evident at 2200 UTC. As forecast time increases, the northeastward extent of the smoke plume increases, generally matching observations (Figs. 3a–c). The coverage of large vertically integrated smoke concentration values (smoke > 100 mg m^{-2}) somewhat exceeds the smoke plumes evident from visible satellite data and AOD retrievals. Smoke aerosol heights differ significantly from fire to fire with the Bush fire generating smoke up to 7 km (MSL) while forecast smoke from the Mangum fire reaches in excess of 9 km (Figs. 3d–f). For all fires, the heights of the smoke plumes increase as a function of

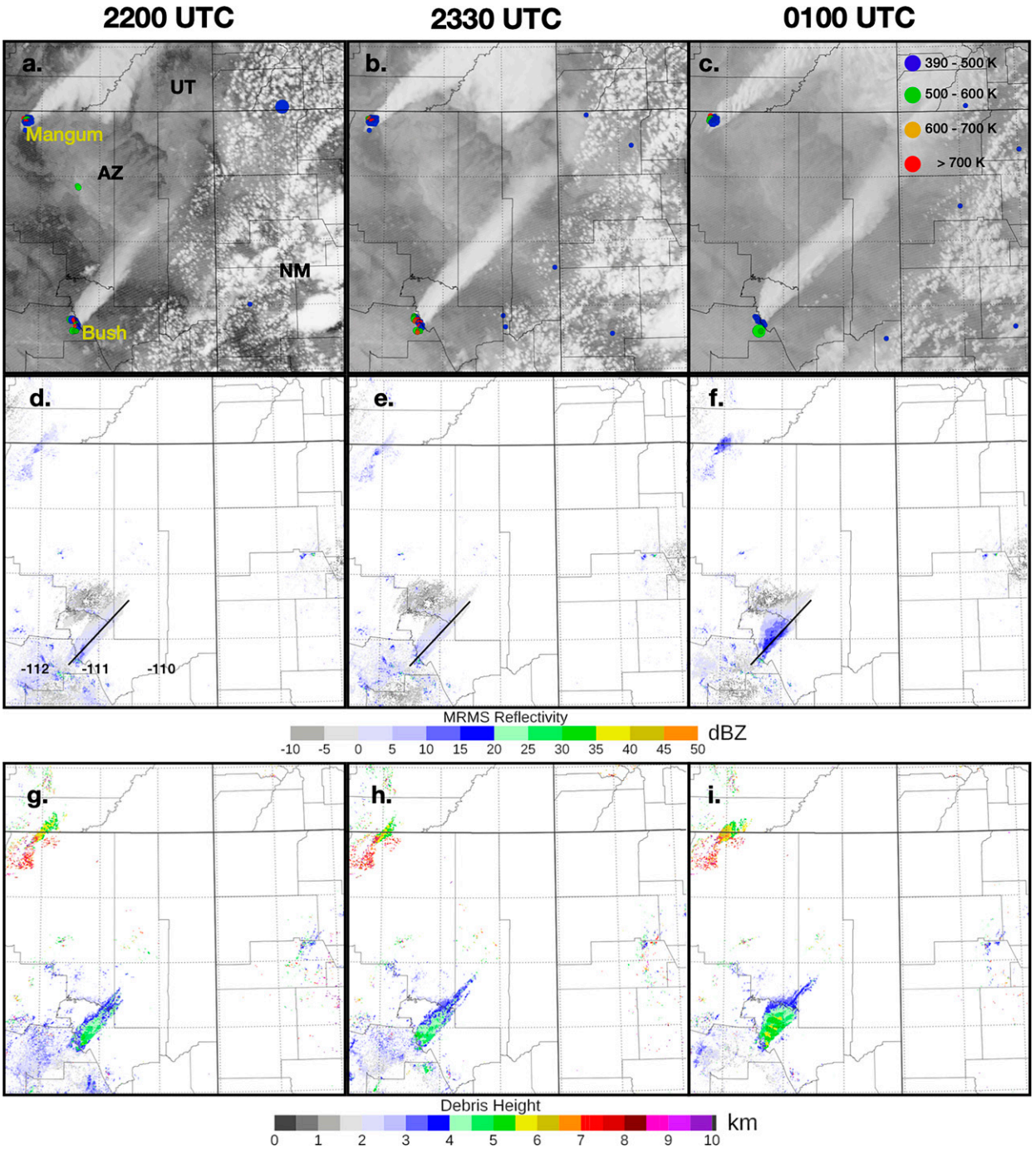

FIG. 2. (a)–(c) *GOES-17* visible (0.47 μm) imagery at 2200, 2330, and 0100 UTC 16–17 Jun 2020. Corresponding "hotspot" detections from *GOES-16* at these times are also provided with colors representing their retrieved temperature and their size as a representation of their coverage. The size of the dots does not directly represent the actual fire size but is plotted to show the locations of smaller vs larger detections. (d)–(f) Maximum column MRMS reflectivity for nonprecipitation returns at the same times. (g)–(i) The corresponding maximum debris heights are shown. MRMS debris height represents the highest level where reflectivity is greater than −5 dBZ. The diagonal line on the reflectivity plots represents the cross-section location used in Fig. 4 below.

forecast time. Other areas of upper level aerosols also exist in western New Mexico (NM) and southern CO and are associated with fires occurring prior to the WoFS-Smoke cycling period.

Using an ensemble approach provides the opportunity for probabilistic forecasts of smoke plume extent and intensity. The probability of total column smoke greater than 50 mg m^{-2} at the analysis time, and 90-, and 180-min forecasts thereafter, is

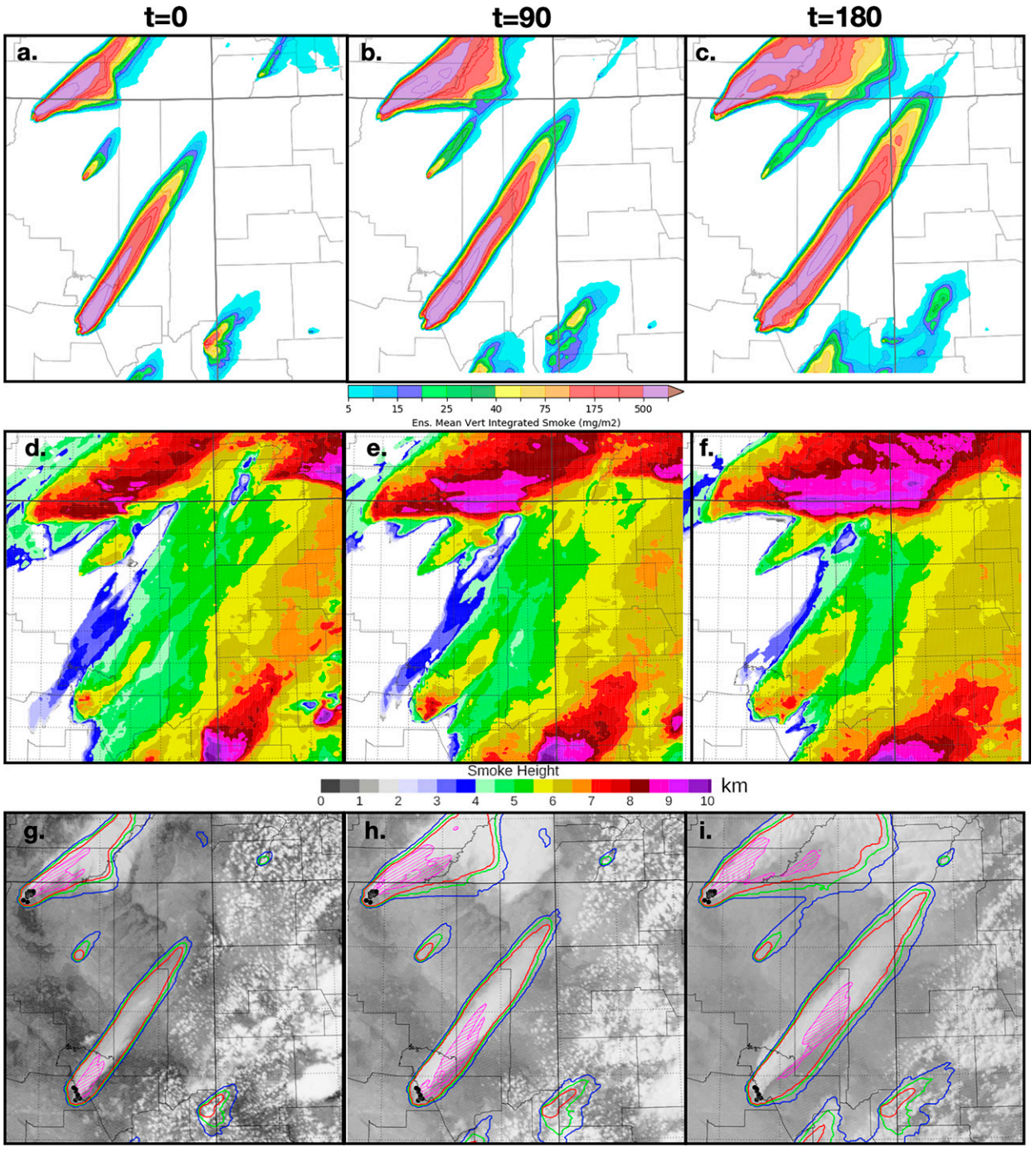

FIG. 3. (a)–(c) Ensemble mean vertically integrated PM2.5 (smoke) forecasts from WoFS-smoke initialized at 2200 UTC for 0-, 90-, and 180-min forecast times. (d)–(f) Maximum smoke aerosol height defined as the maximum level where smoke is greater than 0.1 mg kg^{-1}. Note that the coverage of aerosols appears larger on the height plots since the relatively small total column values for thin layers of smoke do not appear on the top row of plots so the color scale can emphasize smoke plume characteristics. (g)–(i) The probability of vertically integrated PM2.5 (smoke) > 50 mg m^{-2} contours at 10% (blue), 50% (green), and 90% (red) overlaid on *GOES-17* visible imagery valid at each forecast time. Also overlaid in pink is the area where the standard deviation of vertically integrated smoke over each ensemble member for the same forecast times is >200 mg m^{-2}. Black dots indicate the locations of model analyzed hotspots at 2200 UTC.

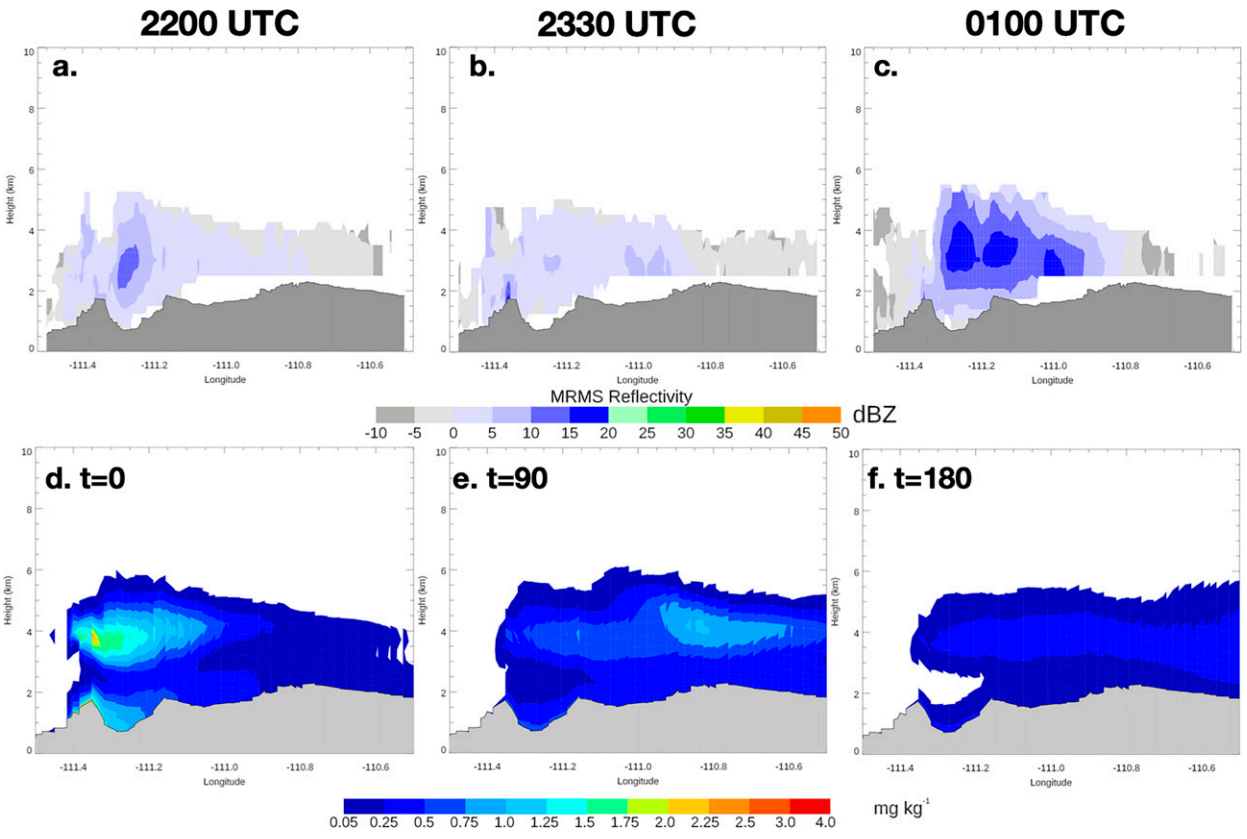

FIG. 4. (a)–(c) Vertical cross sections of MRMS radar reflectivity of the Bush fire debris plume at 2200, 2330, and 0100 UTC 16–17 Jun 2020. Cross sections are computed along the lines shown in Fig. 3. Height is provided in kilometers above sea level and ground elevation is shaded in gray. The corresponding ensemble mean smoke cross-section (d) analysis and (e),(f) forecasts computed along the same paths.

compared against visible observations valid at those times (Figs. 3g–i). High probabilities (>90%) increase as a function of time northeastward consistent with the ensemble mean forecasts and observations. There is little ensemble spread in the spatial extent of smoke > 50 mg m^{-2} for the more intense fires, but somewhat greater spread from the smaller fires. For these fires, variations in the initialization of observed hotspot retrievals make a larger impact and low-level changes in wind speed and direction also become more relevant. While the spatial ensemble spread is generally low, much larger variations in smoke concentrations are evident. To visualize this, the standard deviation of forecast total smoke concentration from each ensemble member is calculated at each forecast time and values greater than 200 mg m^{-2} are overlaid on Figs. 3g and 3i. Standard deviation values exceed 200 mg m^{-2} for the two strongest fires near their origin at the analysis time. The degree of spread increases downstream as forecast time increases. Note that there is minimal spread in forecast smoke aerosol concentrations associated with the upper level smoke in western NM and southern CO. Since much of this smoke is not being generated by the Bush or Mangum fires, there is little potential for spread to occur in the forecast. When comparing smoke forecasts with those of severe weather, the overall spread is generally lower. The spread is driven by the mid- to upper level environmental winds, which are similar from member to member for this case. The movement of fires over the time span being forecast here is small, limiting temporal spread in the forecast smoke plume.

Further verification of WoFS-Smoke forecasts can be performed by comparing vertical cross-sections of forecast smoke with vertical cross sections of radar reflectivity along the same path. While it is understood that this is not a true "apples to apples" comparison, it does give insight into whether or not the vertical profile of forecast smoke is realistic. Figure 4 shows vertical cross sections of MRMS reflectivity corresponding to the lines plotted in Figs. 2d–f at 2200, 2330, and 0100 UTC. Maximum debris injection heights occur near the origin; however, they remain evident at least 2 km above the surface over 100 km downstream. Corresponding WoFS-Smoke ensemble mean cross sections of smoke show a similar spatial pattern, but with several important differences. The forecast smoke plumes generally extend ~1 km higher into the atmosphere than the observed debris, which is consistent with the smaller lighter particles being forecast. The maximum smoke height remains relatively constant at later forecast times, with a smaller drop-off as smoke particles remain in atmosphere longer.

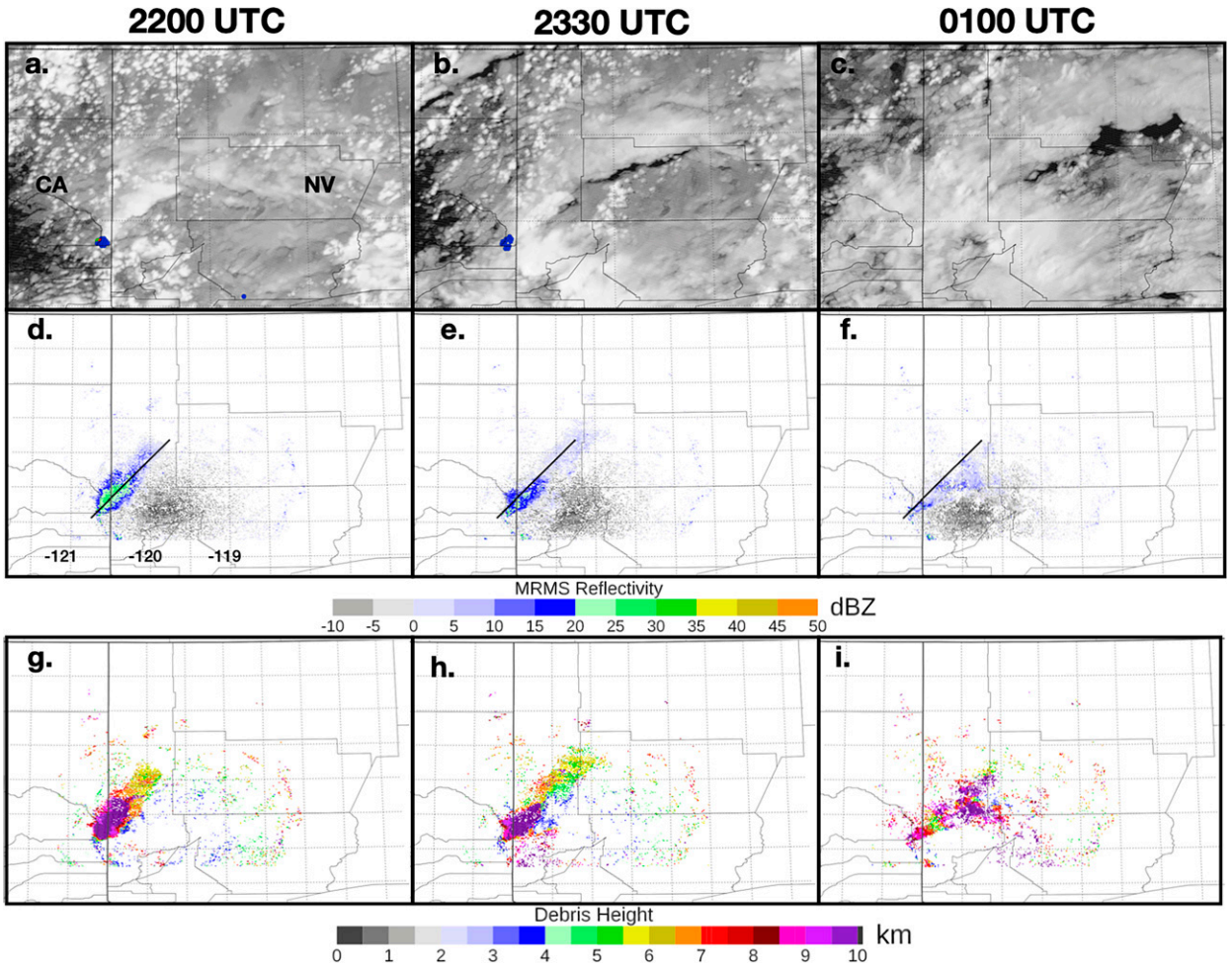

FIG. 5. As in Fig. 2, but for 2200, 2330, and 0100 UTC 15–16 Aug 2020 and from *GOES-17*. Note that the fire in northwestern CA was not detected by available radar observations.

One important difference is the increase in reflectivity at 0100 UTC does not correspond to an increase in forecast smoke. The overall decreasing magnitude of smoke at later forecast times is in part a reflection of increasing ensemble spread, but most members at this time do show a decrease in forecast smoke concentrations (not shown). Recall that *GOES-17* hotspot retrievals associated with the Bush fire indicate a growing fire between 2000 and 0000 UTC (Fig. 1a). This growth trend is not fully taken into account by the system; thus, the size and intensity of the fire cannot increase once the forecast is initiated. As a result, WoFS-Smoke likely under-forecasts the amount of smoke in the atmosphere at later forecast times.

b. 15 August 2020: Loyalton fire

On 14 August a large fire, known as the Loyalton fire, originated in eastern CA from a lightning strike in the Tahoe National Forest, which grew significantly in size on 15 August eventually burning 50 000 acres of tall grass and timber (Fig. 1b). While this fire was not as large as many others during this summer, it was unusual in that pyroCb initiated by the fire went on to spawn at least three tornadoes between 2130 and 2241 UTC, 2 of which were rated EF1 (https://www.ncdc.noaa.gov/stormevents/). This was the first known instance of a tornado warning issued for tornado that formed under these conditions in pyroCb (http://mesonet.agron.iastate.edu/wx/afos/p.php?pil=TORREV&e=202008152135).

GOES-17 visible imagery at 2200 UTC and hotspot detections indicates the location of this fire as well as its associated smoke plume, which advects downstream in a northerly and northeasterly direction (Fig. 5a). The fire size, intensity, and coverage of this smoke plume is generally lower than those observed for the AZ case (Table 1). Smoke plumes increase in size and thickness as a function of time with smoke generated by the Loyalton fire present across all of northern Nevada (NV) by 0100 UTC (Figs. 5b,c). MRMS radar reflectivity observations at 2200 UTC indicate substantial amounts of debris being lofted into the atmosphere near the fire's origin (>25 dBZ) with lower concentrations detectable over 50 km downstream (Fig. 5d). The amount of lofted debris decreases as a function of time and

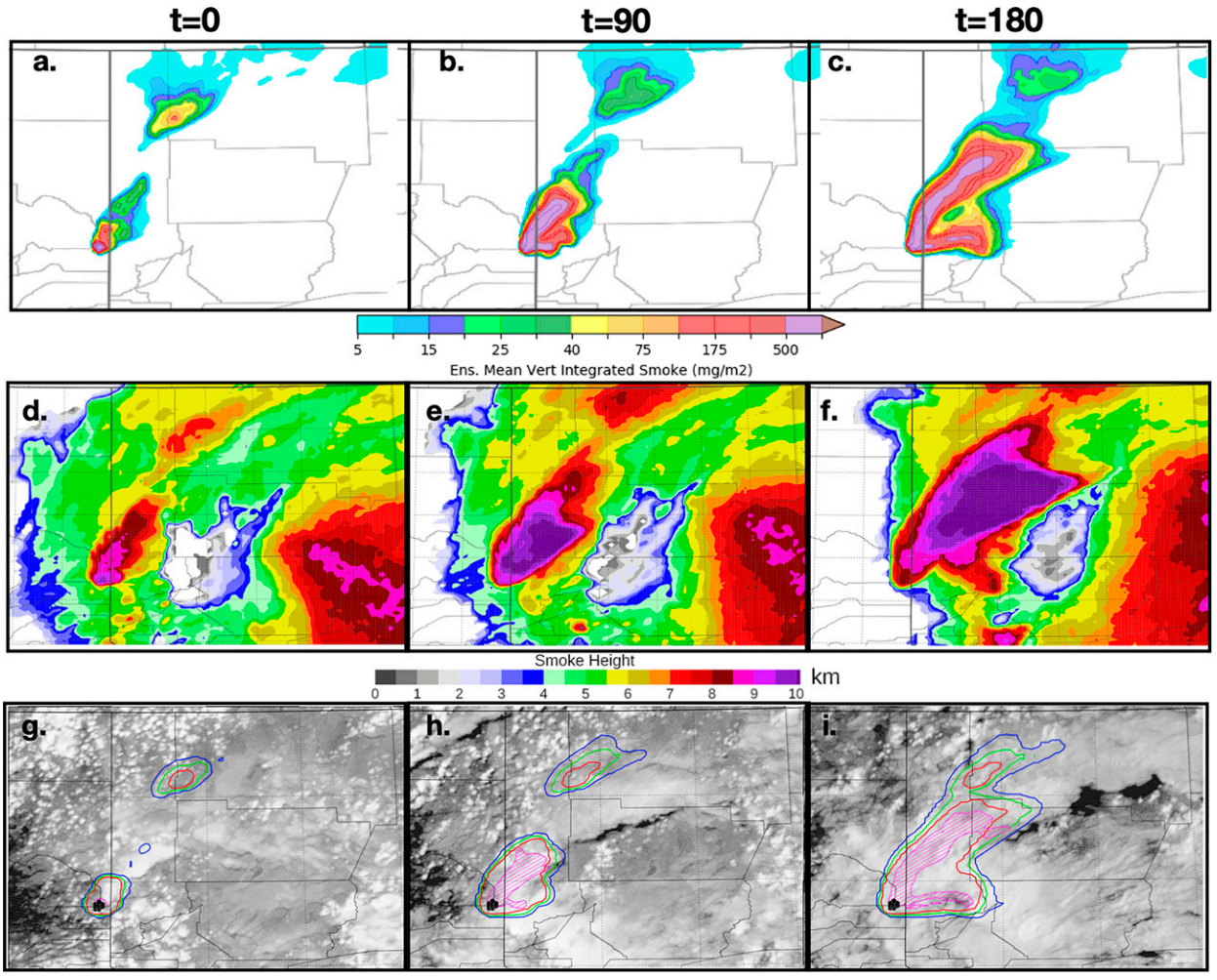

FIG. 6. As in Fig. 3, but for 2200, 2330, and 0100 UTC 15–16 Aug 2020.

is barely evident from radar data at 0100 UTC (Fig. 5f). This strongly indicates the weakening of the fire near its origin during this period, which is consistent with the rapid decrease in *GOES-17* FRP after 2300 UTC (Fig. 1b). Corresponding debris plume heights reach in excess of 10 km above sea level (>8 km above the surface) indicating strong updrafts are present, which are necessary to loft debris to these altitudes (Figs. 5g–i). Recall that the overall FRP intensity is less than observed for the other two cases, but that the *SNPP* retrieved very high values at 2115 UTC (Table 1). The high values at 2115 UTC may be in response to intense small scale fire features not resolvable from GOES data, but which contribute to the intense updrafts present at 2200 UTC. The amount of debris in the atmosphere decreases as a function of time though some remains present in the atmosphere well above the surface at 0100 UTC. The development of pyroCb also introduced liquid and ice hydrometeors into the atmosphere, which are also detectable from radar. However, analysis of the polarimetric variables indicated that the primary source of radar returns are the debris (not shown).

Since WoFS-Smoke currently lacks full coupling between smoke aerosols and the cloud microphysics scheme, it is unable to create pyroCb. At 2200 UTC, a relatively small area of smoke extends northeast of the Loyalton fire, which grows in size and smoke aerosol concentration at later forecast times (Figs. 6a–c). The overall shape and extent of the forecast smoke plume is consistent with the satellite observations in Fig. 5. Smoke generated from the Loyalton fire is forecast to extend over 10 km above sea level with the height generally increasing as a function of time (Figs. 6d–f). A large area of upper-level smoke is also forecast in NV, which is left over from fires occurring during the previous days. The spatial ensemble spread in smoke forecasts is relatively small, but both the northeastward and later eastward transport of the smoke are well forecast during this period (Figs. 6g–i). Greater spread again exists in the forecast intensity of the smoke plume at later forecast times.

Comparing observed radar reflectivity and forecast smoke concentrations during this period reveals several substantial differences between the two. At 2200 UTC, radar observations

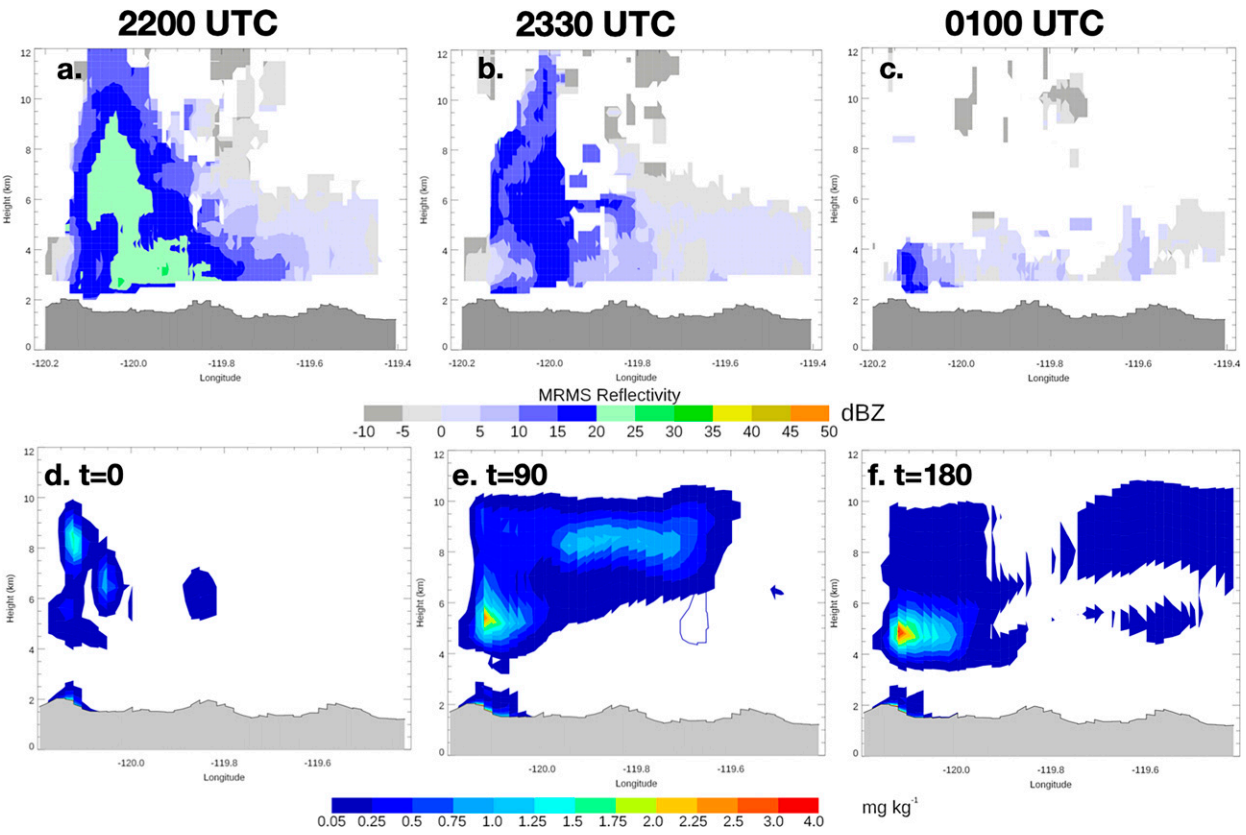

FIG. 7. As in Fig. 4, but for MRMS radar reflectivity and WoFS-smoke forecasts initialized at 2200 UTC 15 Aug 2020.

indicate detectable debris being lofted over 12 km MSL (~10 km AGL) with reflectivity values in excess of 20-dBZ indicating large debris concentrations aloft (Fig. 7). Prior reflectivity values at 2100 UTC were even greater (>40 dBZ, not shown). Observed reflectivity is already decreasing in height and intensity by 2200 UTC and becomes quite low by 0100 UTC. This strongly indicates the fire has weakened significantly by this time and is generating much less lofted debris. Recall that the number of *GOES-17* hotspot detections also decreases rapidly after 2300 UTC. WoFS-Smoke forecasts along the same cross section paint a somewhat different picture. At 2200 UTC, overall smoke concentrations near the fire are quite low compared to the amount of debris in the air (Figs. 7a,d). By 2330 UTC, forecast smoke concentrations have increased considerably with a plume extending well downstream of the fire. The radar data indicates falling debris over this region while smoke remains consolidated much higher in the atmosphere (Figs. 7b,c). This pattern continues to 0100 UTC when mostly low-level debris remains, but upper-level aerosols remain. Note that WoFS-Smoke is still generating large amounts of smoke at 0100 UTC despite the strong evidence from both satellite and radar data that the fire is weakening. Given that the model assumes a persistence approach to the future intensity of the fire, over forecasting of smoke associated with a weakening fire would be expected.

The general lack of smoke in the 2200 UTC analysis indicates that WoFS-Smoke is not fully initializing the fire. Few hotspot retrievals exist in VIIRS and MODIS data prior to 2100 UTC due to a combination of clouds interfering with the retrievals and the small size of the fire (Fig. 1b). Only the *SNPP* overpass at ~2115 UTC generates more than a few retrievals. These data are ingested into WoFS-Smoke at 2200 UTC, so smoke generated from the fire prior to this time is under forecast. More frequent ingesting of hotspot retrievals would be required to properly "spin up" small, rapidly fires such as the one described here. This case represents an example of where assimilating *GOES-17* hotspot retrievals prior to 2200 UTC could improve the overall forecast.

c. *14 October 2020: Cameron Peak and east troublesome fires*

Several large wildfires occurred between August and October 2020 in northern CO. One was a wildfire that started in the Medicine Bow Mountains west of Fort Collins on 13 August burning conifer trees and generating very large amounts of smoke throughout the period. The fire varied in intensity and coverage during this period, but was very intense on 14 October with many hotspot retrievals being made from multiple satellites (Fig. 1c). On this day, the fire lofted large amounts of smoke aerosols and debris deep into the atmosphere and at times generated pyroCu clouds that reached up to 12 km above

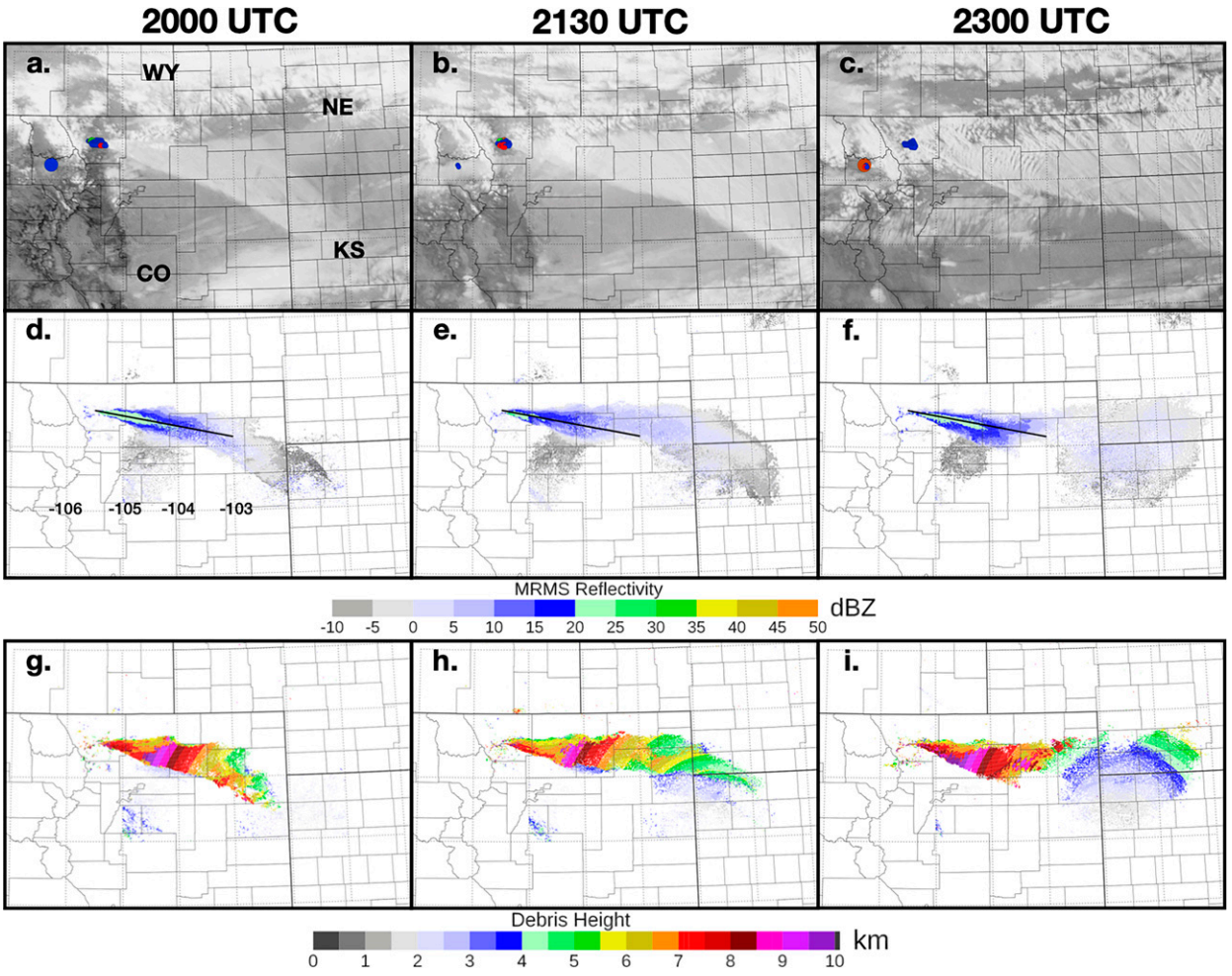

FIG. 8. As in Fig. 2, but for 2000, 2130, and 2300 UTC 14 Oct 2020.

the surface. Another large wildfire originated in northern CO on 14 October northeast of Kremmling, CO, and was known as the East Troublesome fire. The location of this fire is only ~50 km south of the Cameron Peak fire. At 2100 UTC, a large smoke plume is evident emanating primarily from the Cameron Peak fire and is spreading eastward into Kansas and Nebraska (Fig. 8a). It continues to increase in size during the following 3 h (Figs. 8a–c). Corresponding radar observations show a well-defined debris plume extending from the fire into eastern CO (Figs. 8d–f). Reflectivity values in excess of 20 dBZ are evident nearly 200 km downstream of the fire at 2000 and 2300 UTC indicating substantial amounts of debris being lofted into the atmosphere. Corresponding maximum debris heights are somewhat difficult to discern due to radar coverage, but are in excess of 6 km above sea level in a large portion of the plume (Figs. 8g–i). Values up to 10 km near the areas of maximum reflectivity values are also observed (Figs. 8g–i).

Smoke forecasts initialized at 2000 UTC show a northwest–southeast smoke plume originating from the Cameron Peak fire that increases substantially in size as forecast time increases (Figs. 9a–c). By 2000 UTC, hotspot retrievals from four different overpasses have been ingested into the system. Maximum smoke heights associated with these plumes extend 7 km above sea level over a large area (Figs. 9d–f). The smoke height forecast plots also show the expansive coverage of smoke in much of CO from fires during the previous days and weeks. The overall spatial extent of the smoke plume does not vary significantly from member to member, but the spread in smoke concentrations is evident (Figs. 9g–i). The variations in smoke concentrations are maximized near the origin of the fire and decrease downstream. Little variation exists in smoke aerosol concentrations not directly associated with this smoke plume. Cross sections of radar reflectivity and forecast smoke reveal several differences. At 2000 UTC, radar reflectivity greater than 20 dBZ reaches up to 6 km above sea level near the fire, decreasing to ~4 km farther downstream (Fig. 10a). The pattern is similar at later forecast times (Figs. 10b,c). The maximum debris heights near the fire are only 7–8 km, but reach 9 km farther downstream. This is a result of the radar scan modes present at this time. The radar nearest the fire was operating in clear-air mode; thus, it

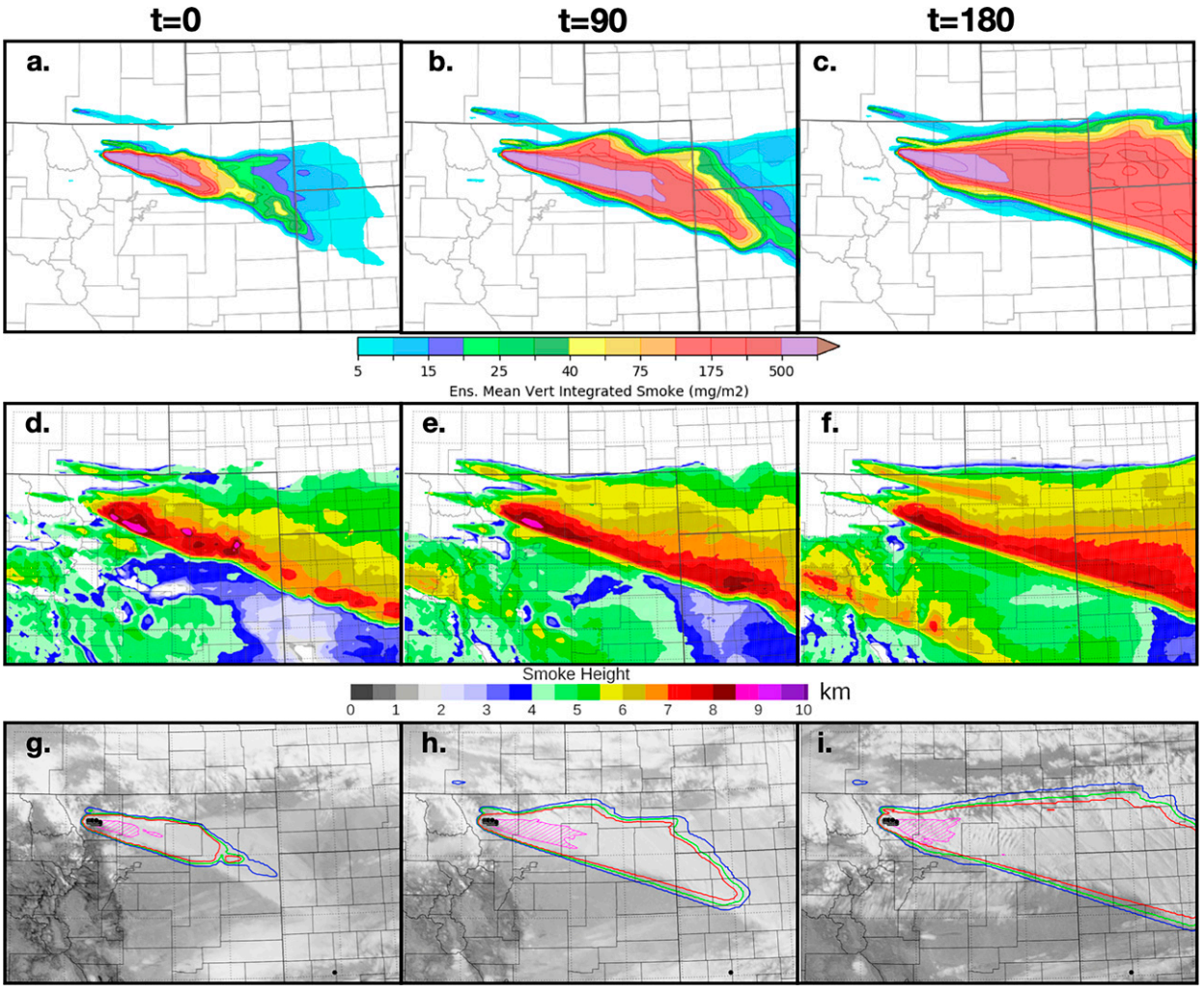

FIG. 9. As in Fig. 3, but for 2000, 2130, and 2300 UTC 14 Oct 2020. The artifacts in the radar heights values are a result of debris being detectable above the highest radar scan elevation at a particular location.

did not observe the upper portion of the debris plumes. Forecast smoke during this period only extends up to 6.5 km; though remains aloft farther downstream as it is slower to fall out of the atmosphere (Figs. 10d–f). Downstream smoke also increases with forecast time, which is consistent with satellite observations (Fig. 8).

Large concentrations of smoke aerosols can have measurable impacts to the surrounding thermodynamic environment, which can be forecasted using WoFS-Smoke through the link between smoke aerosols and the radiation parameterization scheme (RRTMG). The forecast 2-m temperature from an experiment that include smoke (SMOKE) and one that does not (CNTL) are compared to show this impact. Figure 11 shows ensemble mean 2-m temperature at 2200 UTC and for 90 and 180-min forecasts thereafter for both experiments. Sustained wind speed and direction at 10 m above the surface are also provided. In both experiments, a large pool of cool (<10°C) air exists in the northern portion of the domain that is being transported southward behind a cold front located in southern CO. Comparing observed surface temperature from the ASOS sites to the forecast temperature shows that the model has a warm bias over much of this region. This bias is most evident in CNTL near the origin of the fire (black circle) where two ASOS sites are reporting 2-m temperatures over 5°C cooler than the forecast values at 2130 and 2300 UTC (Figs. 10b,c). However, the forecast temperature from SMOKE at these times is substantially cooler (Figs. 10e,f). The difference between 2-m temperature for these experiments (SMOKE-CNTL) shows a broad area of cooling at the surface in SMOKE associated with the smoke plume (Figs. 10g–i). The area of this cooling increases as a function of forecast time and is maximized near the fire's origin where smoke aerosol concentrations are greatest. For this case, the addition of smoke aerosols to WoFS cools forecasts of surface temperature more than 5°C in areas where total column smoke is greater than 500 mg m^{-2}. Bias (ASOS − model) and root-mean-square error (RMSE) for 2-m temperature in this

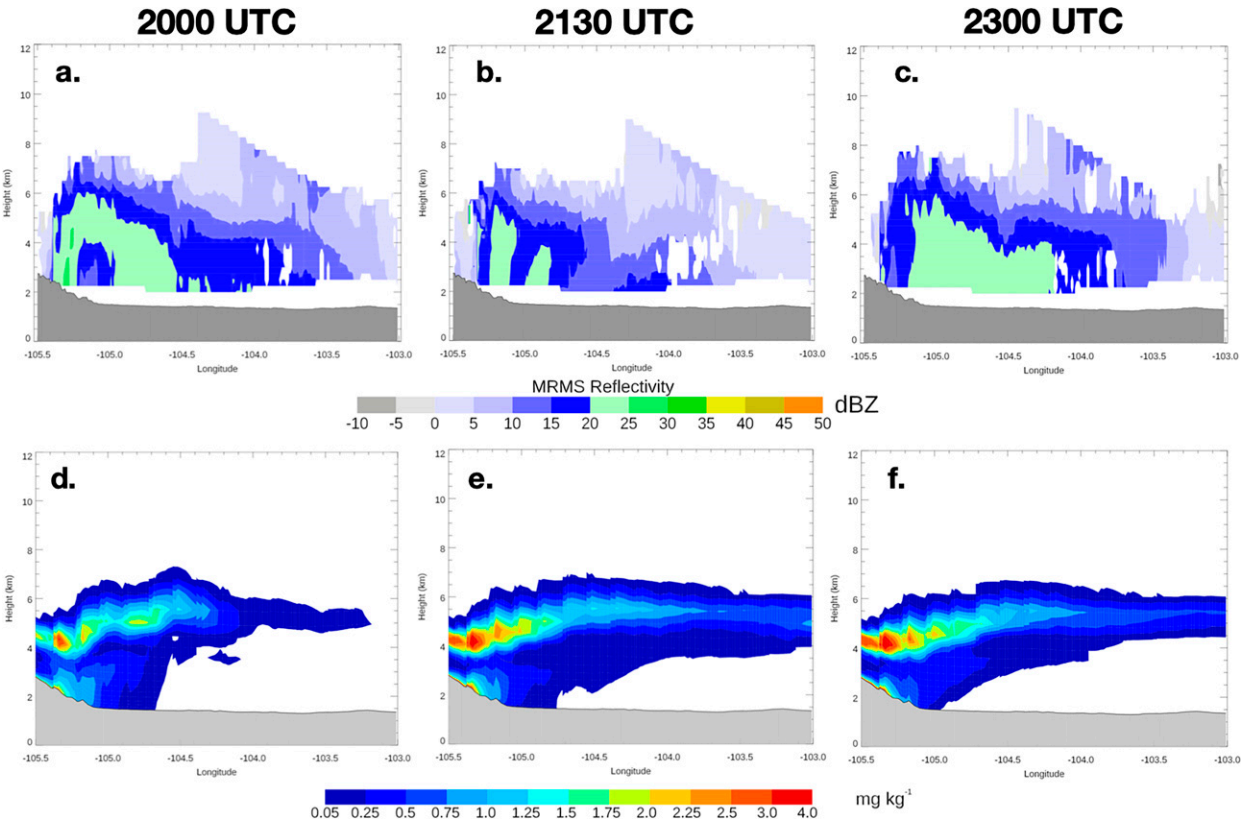

FIG. 10. As in Fig. 4, but for MRMS radar reflectivity and WoFS-smoke forecasts initialized at 2000 UTC 14 Oct 2020.

domain are also calculated at 5-min intervals for the 3-h forecast initiated at 2000 UTC (Fig. 12). The domain encompasses 20 ASOS sites that report observations during this period. Both experiments have a warm bias, but SMOKE reduces this bias by ~0.5°C. Corresponding RMSE is reduced by nearly 1.0°C. The statistics are calculated individually for each member and the error bars in Fig. 12 indicate the standard deviation of bias and RMSE calculated over all 18 forecast members at a particular time. For RMSE in particular, the differences in the mean error generally lie outside the ensemble spread.

5. Conclusions

The goal of this work was to create a rapid cycling, ensemble data assimilation and forecasting system for smoke aerosols (PM2.5) generated from wildfires. To accomplish this goal, the existing WoFS, which was designed to generate short-term severe weather forecasts, is extended to also generate forecasts of smoke. This was accomplished by ingesting FRP retrievals from polar orbiting satellites using techniques developed for the HRRR-Smoke system. The resulting WoFS-Smoke generated reasonably accurate short-range forecasts of smoke coverage for three wildfire cases. Forecast smoke was broadly consistent with satellite-based aerosol observations, but important differences were apparent. In both the 16 June and 14 October cases, 0–3-h probabilistic analyses and forecasts of vertically integrated smoke plumes matched well with observations. However, the amount of smoke generated by the Loyalton fire was significantly under analyzed. Only ingesting polar orbiting data resulted most of the simulated smoke concentrations being generated from a single overpass at 2115 UTC. As with severe weather forecasting, multiple inputs over a period of time are required to accurately spin up a feature within the system. As a result, existing smoke associated with this fire is not fully analyzed. Despite the analyzed smoke being underforecast, the 3-h forecast of smoke for this case was substantially over forecast. Both satellite and radar data indicate a very intense fire at ~2200 UTC, but the same data also show it weakening quickly thereafter. Since WoFS-Smoke assumes the fire intensity changes little during this time period, it does not take into account the rapid weakening of the fire after 2300 UTC.

Comparisons between forecast maximum aerosol heights and the observed maximum debris height from radar data provide insight into the accuracy of the vertical distribution of forecast smoke. For 2 cases, radar debris heights were lower than maximum aerosol heights, which would be expected as radar detectable debris should fall out of the atmosphere much faster than smoke aerosols. For the Loyalton fire in CA and the fires in CO, radar observed debris is present higher in the atmosphere than forecast smoke indicating that WoFS-Smoke still has room for improvement. Finally, verification of

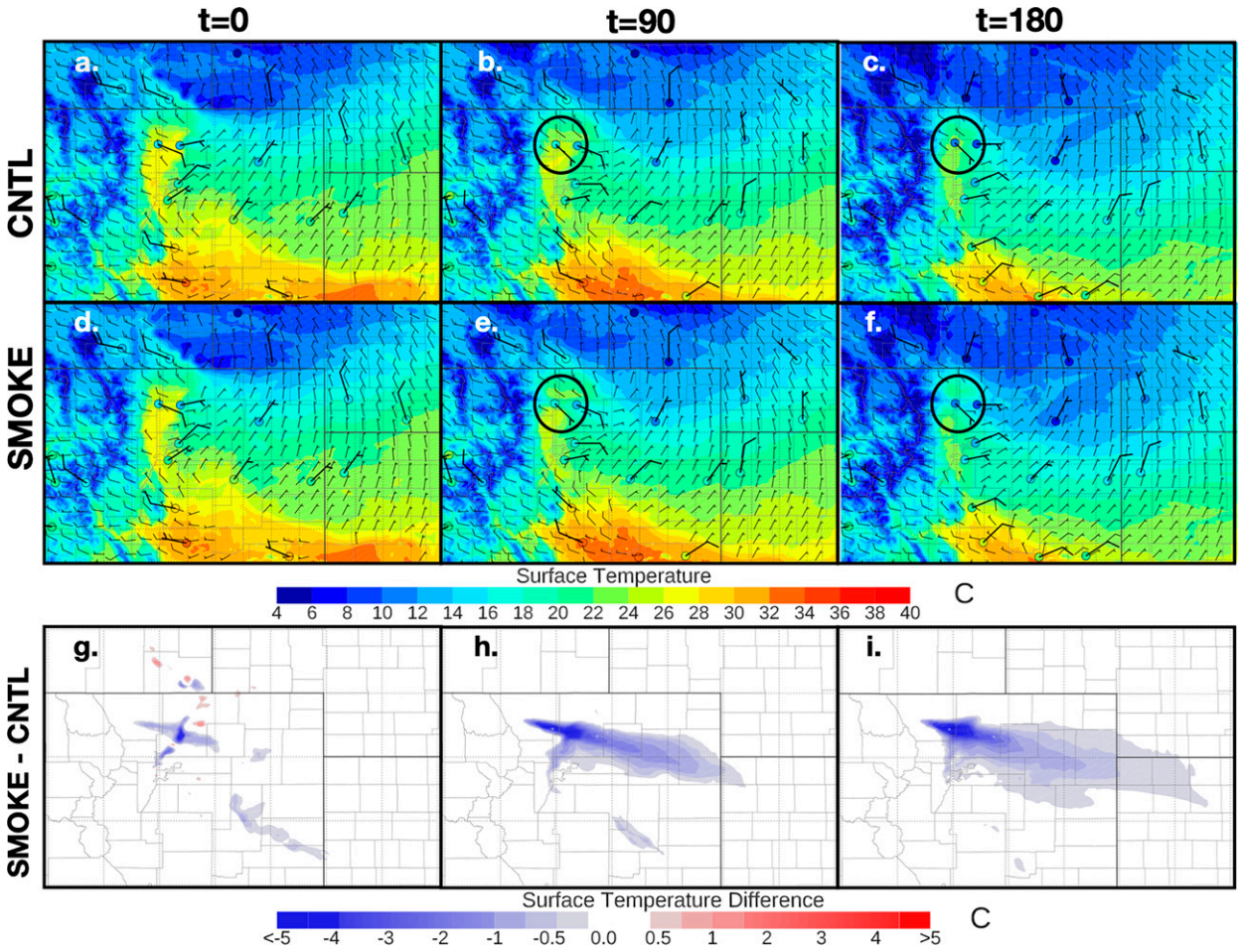

FIG. 11. Forecast ensemble mean 2-m temperature for 0-, 90-, and 180-min forecasts initiated at 2000 UTC 14 Oct for the (a)–(c) CNTL and (d)–(f) SMOKE experiments. Dots indicate location and temperature value for each ASOS site in the domain. Wind speed and direction at 10 m above the surface is also provided, with short barbs indicating 5 m s^{-1} and long barbs indicating 10 m s^{-1}. (g)–(i) The ensemble mean difference in 2-m temperature (SMOKE − CNTL) at each forecast time.

surface temperature forecasts for the 14 October case reveals that including smoke in the forecast model reduces temperature bias and error in areas where thick smoke was evident. This improvement remained consistent throughout the entire 3-h forecast period.

There remains much room for improvement to the prototype data assimilation and forecasting system outlined here. Most importantly, high temporal resolution FRP retrievals are not yet being ingested. The results from these example cases indicated several examples when ingesting these data more frequently as well as including short term trend information would likely improve the short-term smoke forecasts. Another limitation is the lack of ensemble spread in the spatial distribution of thick smoke. Since these wildfires are mostly fixed sources of smoke for the spatial and temporal resolution studied here, smoke is continuously injected into the atmosphere at that location. This often occurs in environments where there is low spread in the forecast wind fields, limiting the differences in the spatial extent of smoke downstream. The uncertainties added to the FRP retrievals and smoke initial conditions did add significant ensemble spread in the amount of smoke forecast, but for the large fires, these variations are generally contained within the same spatial area. Finally, there is the lack of coupling between fire heat, smoke aerosols, and cloud microphysics. In many strong wildfire cases including those shown here, the development of pyroCu is common. The current system does not increase CCN within the smoke plume, which might lead to the formation of liquid and ice hydrometeors. Also, updrafts produced by extreme heat are not analyzed, further limiting potential cloud development within the model. Ideally, these would all be interlinked, which would significantly improve the overall forecast especially in cases like the Loyalton fire. Many additional upgrades to WoFS-Smoke are planned and include an AOD assimilation capability, ingesting current and future GOES-R satellite FRP retrievals, and improved links between wildfire characteristics and the surrounding environment.

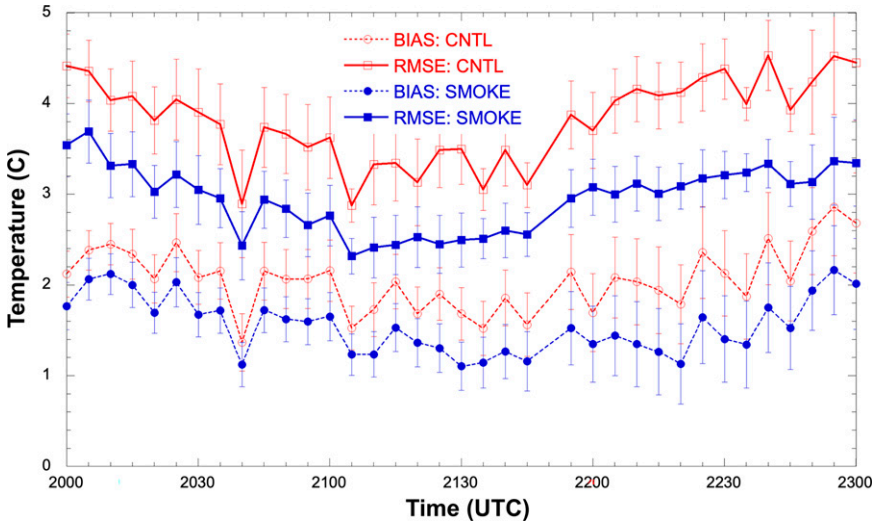

FIG. 12. Bias (ASOS − model) and RMSE of 2-m temperature for CNTL and SMOKE for a forecast initiated at 2000 UTC calculated using the ASOS sites located within the domain plotted in Fig. 11. Error bars represent the standard deviation of bias or RMSE calculated over all ensemble members at a particular forecast time.

Acknowledgments. This research was funded in part by the NOAA Warn-on-Forecast project. Additional funding was provided the under the NOAA–University of Oklahoma Cooperative Agreements NA16OAR4320115 and NA21OAR4320204, U.S. Department of Commerce, and the CIMMS Directors Discretionary Research Fund (DDRF). Support for WoF computing resources was provided by Mr. Gerry Creager. Internal reviews by Dr. Nusrat Yussouf and Dr. Patrick Skinner were instrumental at improving aspects of this manuscript. HRRRE initial and boundary conditions for this work were provided by the Global Systems Laboratory as part of real-time experiments in 2020. We also thank NOAA's Joint Polar Satellite System Proving Ground and Risk Reduction program for funding and the rest of the HRRR-Smoke team and collaborators for helping with the model development.

Data availability statement. The WoFS-smoke output used from these experiments are available at https://wof.nssl.noaa.gov/research_retro/. The raw data and code used to generate these results are available from the authors upon request.

REFERENCES

Ahmadov, R., and Coauthors, 2017: Using VIIRS Fire Radiative Power data to simulate biomass burning emissions, plume rise and smoke transport in a real-time air quality modeling system. *2017 IEEE Int. Geoscience and Remote Sensing Symp. (IGARSS)*, Fort Worth, TX, IEEE, 2806–2808, https://doi.org/10.1109/IGARSS.2017.8127581.

Alexander, C. R., and Coauthors, 2018: Development of the High-Resolution Rapid Refresh Ensemble (HRRRE). *22nd Conf. on Integrated Observing and Assimilation Systems for the Atmosphere, Oceans, and Land Surface (IOAS-AOLS)*, Austin, TX, Amer. Meteor. Soc., 11.3, https://ams.confex.com/ams/98Annual/webprogram/Paper335526.html.

Anderson, J. L., 2009: Spatially and temporally varying adaptive covariance inflation for ensemble filters. *Tellus*, **61A**, 72–83, https://doi.org/10.1111/j.1600-0870.2008.00361.x.

Banta, R. M., L. D. Olivier, E. T. Holloway, R. A. Kropfli, B. W. Bartram, R. E. Cupp, and M. J. Post, 1992: Smoke-column observations from two forest fires using Doppler lidar and Doppler radar. *J. Appl. Meteor.*, **31**, 1328–1349, https://doi.org/10.1175/1520-0450(1992)031<1328:SCOFTF>2.0.CO;2.

Benjamin, S. G., and Coauthors, 2016: A North American hourly assimilation and model forecast cycle: The Rapid Refresh. *Mon. Wea. Rev.*, **144**, 1669–1694, https://doi.org/10.1175/MWR-D-15-0242.1.

Coakley, J. A., Jr., R. D. Cess, and F. B. Yurevich, 1983: The effect of tropospheric aerosols on the Earth's radiation budget: A parameterization for climate models. *J. Atmos. Sci.*, **40**, 116–138, https://doi.org/10.1175/1520-0469(1983)040<0116:TEOTAO>2.0.CO;2.

Coen, J. L., M. Cameron, J. Michalakes, E. G. Patton, P. J. Riggan, and K. M. Yedinak, 2013: WRF-Fire: Coupled weather-wildland fire modeling with the Weather Research and Forecasting Model. *J. Appl. Meteor. Climatol.*, **52**, 16–38, https://doi.org/10.1175/JAMC-D-12-023.1.

Csiszar, I., W. Schroeder, L. Giglio, E. Ellicott, K. P. Vadrevu, C. O. Justice, and B. Wind, 2014: Active fires from the Suomi NPP Visible Infrared Imaging Radiometer Suite: Product status and first evaluation results. *J. Geophys. Res. Atmos.*, **119**, 803–816, https://doi.org/10.1002/2013JD020453.

Dozier, J., 1981: A method for satellite identification of surface temperature fields of subpixel resolution. *Remote Sens. Environ.*, **11**, 221–229, https://doi.org/10.1016/0034-4257(81)90021-3.

Freitas, S. R., K. M. Longo, and M. O. Andreae, 2006: Impact of including the plume rise of vegetation fires in numerical simulations of associated atmospheric pollutants. *Geophys. Res. Lett.*, **33**, L17808, https://doi.org/10.1029/2006GL026608.

——, ——, R. Chatfield, D. Latham, M. Dias, and M. O. Andreae, 2007: Including the sub-grid scale plume rise of

vegetation fires in low resolution atmospheric transport models. *Atmos. Chem. Phys.*, **7**, 3385–3398, https://doi.org/10.5194/acp-7-3385-2007.

Fromm, M. D., A. Tupper, D. Rosenfeld, R. Servranckx, and R. McRae, 2006: Violent pyro-convective storm devastates Australia's capital and pollutes the stratosphere. *Geophys. Res. Lett.*, **33**, L05815, https://doi.org/10.1029/2005GL025161.

——, D. T. Lindsey, R. Servranckx, G. Yue, T. Trickl, R. Sica, and S. Godin-Beekmann, 2010: The untold story of pyrocumulonimbus. *Bull. Amer. Meteor. Soc.*, **91**, 1193–1210, https://doi.org/10.1175/2010BAMS3004.1.

——, G. Kablick III, and P. Caffrey, 2016: Dust-infused baroclinic cyclone storm clouds: The evidence, meteorology, and some implications. *Geophys. Res. Lett.*, **43**, 12 643–12 650, https://doi.org/10.1002/2016GL071801.

Gaspari, G., and S. E. Cohn, 1999: Construction of correlation functions in two and three dimensions. *Quart. J. Roy. Meteor. Soc.*, **125**, 723–757, https://doi.org/10.1002/qj.49712555417.

Giglio, L., L. Boschetti, D. Roy, A. A. Hoffmann, and M. Humber, 2016: Collection 6 MODIS burned area product user's guide version 1.0. NOAA/USGS, 26 pp., https://modis-land.gsfc.nasa.gov/pdf/MODIS_C6_BA_User_Guide_1.0.pdf.

——, ——, ——, M. L. Humber, and C. O. Justice, 2018: The Collection 6 MODIS burned area mapping algorithm and product. *Remote Sens. Environ.*, **217**, 72–85, https://doi.org/10.1016/j.rse.2018.08.005.

Ginoux, P., M. Chin, I. Tegen, J. M. Prospero, B. Holben, O. Dubovik, and S.-J. Lin, 2001: Sources and distributions of dust aerosols simulated with the GOCART model. *J. Geophys. Res.*, **106**, 20 255–20 273, https://doi.org/10.1029/2000JD000053.

Grell, G. A., S. E. Peckham, S. McKeen, R. Schmitz, G. Frost, W. C. Skamarock, and B. Eder, 2005: Fully coupled "online" chemistry within the WRF model. *Atmos. Environ.*, **39**, 6957–6975, https://doi.org/10.1016/j.atmosenv.2005.04.027.

Hong, S.-Y., Y. Noh, and J. Dudhia, 2006: A new vertical diffusion package with an explicit treatment of entrainment processes. *Mon. Wea. Rev.*, **134**, 2318–2341, https://doi.org/10.1175/MWR3199.1.

Hu, M., H. Shao, D. Stark, K. Newman, C. Zhou, and X. Zhang, 2016: Gridpoint Statistical Interpolation (GSI) user's guide version 3.5. Developmental Testbed Center, 148 pp., https://dtcenter.ucar.edu/com-GSI/users/docs/users_guide/GSIUserGuide_v3.5.pdf.

Janjić, Z. I., 1994: The step-mountain eta coordinate model: Further developments of the convection, viscous sublayer, and turbulence closure schemes. *Mon. Wea. Rev.*, **122**, 927–945, https://doi.org/10.1175/1520-0493(1994)122<0927:TSMECM>2.0.CO;2.

Jones, T. A., and S. A. Christopher, 2009: Injection heights of biomass burning debris estimated from WSR-88D radar observations. *IEEE Trans. Geosci. Remote Sens.*, **47**, 2599–2605, https://doi.org/10.1109/TGRS.2009.2014225.

——, and ——, 2010a: Satellite and radar observations of the 9 April 2009 Texas and Oklahoma grassfires. *Bull. Amer. Meteor. Soc.*, **91**, 455–460, https://doi.org/10.1175/2009BAMS2919.1.

——, and ——, 2010b: Satellite and radar remote sensing of southern plains grassfires: A case study. *J. Appl. Meteor. Climatol.*, **49**, 2133–2146, https://doi.org/10.1175/2010JAMC2472.1.

——, ——, and W. Petersen, 2009: Dual polarimetric radar characteristics of an apartment fire. *J. Atmos. Oceanic Technol.*, **26**, 2257–2269, https://doi.org/10.1175/2009JTECHA1290.1.

——, K. Knopfmeier, D. Wheatley, G. Creager, P. Minnis, and R. Palikonda, 2016: Storm-scale data assimilation and ensemble forecasting with the NSSL experimental Warn-on-Forecast system. Part II: Combined radar and satellite data experiments. *Wea. Forecasting*, **31**, 297–327, https://doi.org/10.1175/WAF-D-15-0107.1.

——, and Coauthors, 2020: Assimilation of *GOES-16* radiances and retrievals into the Warn-on-Forecast System. *Mon. Wea. Rev.*, **148**, 1829–1859, https://doi.org/10.1175/MWR-D-19-0379.1.

Kaufman, Y. J., and Coauthors, 1997: Passive remote sensing of tropospheric aerosol and atmospheric correction for the aerosol effect. *J. Geophys. Res.*, **102**, 16 815–16 830, https://doi.org/10.1029/97JD01496.

——, and Coauthors, 1998a: Smoke, Clouds, and Radiation-Brazil (SCAR-B) experiment. *J. Geophys. Res.*, **103**, 31 783–31 808, https://doi.org/10.1029/98JD02281.

——, R. Kleidman, and M. D. King, 1998b: SCAR-B fires in the tropics: Properties and remote sensing from EOS-MODIS. *J. Geophys. Res.*, **103**, 31 955–31 968, https://doi.org/10.1029/98JD02460.

Kerr, C., L. J. Wicker, and P. S. Skinner, 2021: Updraft-based adaptive assimilation of radial velocity observations in a Warn-on-Forecast System. *Wea. Forecasting*, **36**, 21–37, https://doi.org/10.1175/WAF-D-19-0251.1.

Kleist, D. T., D. F. Parrish, J. C. Derber, R. Treadon, W.-S. Wu, and S. Lord, 2009: Introduction of the GSI into the NCEP Global Data Assimilation System. *Wea. Forecasting*, **24**, 1691–1705, https://doi.org/10.1175/2009WAF2222201.1.

Koren, I., L. A. Remer, Y. J. Kaufman, Y. Rudich, and J. V. Martins, 2007: On the twilight zone between clouds and aerosols. *Geophys. Res. Lett.*, **34**, L08805, https://doi.org/10.1029/2007GL029253.

Lakshmanan, V., T. Smith, G. J. Stumpf, and K. Hondl, 2007: The Warning Decision Support System–Integrated Information. *Wea. Forecasting*, **22**, 596–612, https://doi.org/10.1175/WAF1009.1.

Lareau, N. P., and C. B. Clements, 2016: Environmental controls on pyrocumulus and pyrocumulonimbus initiation and development. *Atmos. Chem. Phys.*, **16**, 4005–4022, https://doi.org/10.5194/acp-16-4005-2016.

——, N. J. Nauslar, and J. T. Abotzoglou, 2018: The Carr Fire Vortex: A case of pyrotornadogenesis? *Geophys. Res. Lett.*, **45**, 13 107–13 115, https://doi.org/10.1029/2018GL080667.

Lindsey, D., S. Miller, and L. Grasso, 2010: The impacts of the 9 April 2009 dust and smoke on convection. *Bull. Amer. Meteor. Soc.*, **91**, 991–996, https://doi.org/10.1175/2010BAMS2964.1.

Liu, G., H. Shao, J. A. Coakley, J. A. Curry, J. A. Haggerty, and M. A. Tschudi, 2003: Retrieval of cloud droplet size from visible and microwave radiometric measurements during INDOEX: Implication to aerosols' indirect radioactive effect. *J. Geophys. Res.*, **108**, 4006, https://doi.org/10.1029/2001JD001395.

Mansell, E. R., C. L. Ziegler, and E. C. Bruning, 2010: Simulated electrification of a small thunderstorm with two-moment bulk microphysics. *J. Atmos. Sci.*, **67**, 171–194, https://doi.org/10.1175/2009JAS2965.1.

McRae, R. H., J. J. Sharples, S. R. Wilkes, and A. Walker, 2013: An Australian pyro-tornadogenesis event. *Nat. Hazards*, **65**, 1801–1811, https://doi.org/10.1007/s11069-012-0443-7.

Melnikov, V., D. Zrnić, and R. Rabin, 2009: Polarimetric radar properties of smoke plumes: A model. *J. Geophys. Res.*, **114**, D21204, https://doi.org/10.1029/2009JD012647.

Nakanishi, M., and H. Niino, 2006: An improved Mellor–Yamada level-3 model: Its numerical stability and application to a regional prediction of advection fog. *Bound.-Layer Meteor.*, **119**, 397–407, https://doi.org/10.1007/s10546-005-9030-8.

Peace, M., T. Mattner, G. Mills, J. Kepert, and L. McCaw, 2015: Fire-modified meteorology in a coupled fire–atmosphere model. *J. Appl. Meteor. Climatol.*, **54**, 704–720, https://doi.org/10.1175/JAMC-D-14-0063.1.

Peterson, D. A., E. J. Hyer, J. R. Campbell, M. D. Fromm, J. W. Hair, C. F. Butler, and M. A. Fenn, 2015: The 2013 Rim Fire: Implications for predicting extreme fire spread, pyroconvection, and smoke emissions. *Bull. Amer. Meteor. Soc.*, **96**, 229–247, https://doi.org/10.1175/BAMS-D-14-00060.1.

——, ——, ——, J. E. Solbrig, and M. D. Fromm, 2017: A conceptual model for development of intense pyrocumulonimbus in western North America. *Mon. Wea. Rev.*, **145**, 2235–2255, https://doi.org/10.1175/MWR-D-16-0232.1.

Pope, C. A., III, R. T. Burnett, M. J. Thun, E. E. Calle, D. Krewski, K. Ito, and G. D. Thurston, 2002: Lung cancer, cardiopulmonary mortality, and long-term exposure to fine particulate air pollution. *JAMA*, **287**, 1132–1141, https://doi.org/10.1001/jama.287.9.1132.

Potter, B. E., 2012: Atmospheric interactions with wildland fire behaviour—I. Basic surface interactions, vertical profiles and synoptic structures. *Int. J. Wildland Fire*, **21**, 779–801, https://doi.org/10.1071/WF11128.

Powers, J. G., and Coauthors, 2017: The Weather Research and Forecasting Model: Overview, system efforts, and future directions. *Bull. Amer. Meteor. Soc.*, **98**, 1717–1737, https://doi.org/10.1175/BAMS-D-15-00308.1.

Prins, E. M., and W. P. Menzel, 1992: Geostationary satellite detection of biomass burning in South America. *Int. J. Remote Sens.*, **13**, 2783–2799, https://doi.org/10.1080/01431169208904081.

——, and ——, 1994: Trends in South American biomass burning detected with the GOES visible infrared spin scan radiometer atmospheric sounder from 1983 to 1991. *J. Geophys. Res.*, **99**, 16 719–16 735, https://doi.org/10.1029/94JD01208.

——, J. Feltz, W. Menzel, and D. Ward, 1998: An overview of *GOES-8* diurnal fire and smoke results for SCAR-B and 1995 fire season in South America. *J. Geophys. Res.*, **103**, 31 821–31 835, https://doi.org/10.1029/98JD01720.

Reader, T. W., R. Flin, K. Mearns, and B. H. Cuthbertson, 2009: Developing a team performance framework for the intensive care unit. *Crit. Care Med.*, **37**, 1787–1793, https://doi.org/10.1097/CCM.0b013e31819f0451.

Remer, A., and Coauthors, 2005: The MODIS aerosol algorithm, products, and validation. *J. Atmos. Sci.*, **62**, 947–973, https://doi.org/10.1175/JAS3385.1.

Roberts, G., M. J. Wooster, G. L. W. Perry, N. Drake, L.-M. Rebelo, and F. Dipotso, 2005: Retrieval of biomass combustion rates and totals from fire radiative power observations: Application to southern Africa using geostationary SEVIRI imagery. *J. Geophys. Res.*, **110**, D21111, https://doi.org/10.1029/2005JD006018.

Robock, A., 1988: Enhancement of surface cooling due to forest fire smoke. *Science*, **242**, 911–913, https://doi.org/10.1126/science.242.4880.911.

——, 1991: Surface cooling due to forest fire smoke. *J. Geophys. Res.*, **96**, 20869, https://doi.org/10.1029/91JD02043.

Skamarock, W. C., and Coauthors, 2008: A description of the Advanced Research WRF version 3. NCAR Tech. Note NCAR/TN-475+STR, 113 pp., https://doi.org/10.5065/D68S4MVH.

Skinner, P. S., and Coauthors, 2018: Object-based verification of a prototype Warn-on-Forecast system. *Wea. Forecasting*, **33**, 1225–1250, https://doi.org/10.1175/WAF-D-18-0020.1.

Stensrud, D. J., J.-W. Bao, and T. T. Warner, 2000: Using initial condition and model physics perturbations in short-range ensemble simulations of mesoscale convective systems. *Mon. Wea. Rev.*, **128**, 2077–2107, https://doi.org/10.1175/1520-0493(2000)128<2077:UICAMP>2.0.CO;2.

——, and Coauthors, 2009: Convective-scale Warn-on-Forecast system: A vision for 2020. *Bull. Amer. Meteor. Soc.*, **90**, 1487–1500, https://doi.org/10.1175/2009BAMS2795.1.

——, and Coauthors, 2013: Progress and challenges with Warn-on-Forecast. *Atmos. Res.*, **123**, 2–16, https://doi.org/10.1016/j.atmosres.2012.04.004.

Thompson, G., and T. Eidhammer, 2014: A study of aerosol impacts on clouds and precipitation development in a large winter cyclone. *J. Atmos. Sci.*, **71**, 3636–3658, https://doi.org/10.1175/JAS-D-13-0305.1.

Viegas, D. X., 1998: Convective processes in forest fires. *Buoyant Convection in Geophysical Flows*, E. J. Plate et al., Eds., Kluwer and Academic Publishers, 401–420.

Weaver, J. F., J. F. Purdom, and T. L. Schneider, 1995: Observing forest fires with the *GOES-8*, 3.9-μm imaging channel. *Wea. Forecasting*, **10**, 803–808, https://doi.org/10.1175/1520-0434(1995)010<0803:OFFWTI>2.0.CO;2.

——, D. T. Lindsey, D. E. Bikos, C. C. Schmidt, and E. Prins, 2004: Fire detection using *GOES-11* rapid scan imagery. *Wea. Forecasting*, **19**, 496–510, https://doi.org/10.1175/1520-0434(2004)019<0496:FDUGRS>2.0.CO;2.

Wheatley, D. M., K. H. Knopfmeier, T. A. Jones, and G. J. Creager, 2015: Storm-scale data assimilation and ensemble forecasting with the NSSL Experimental Warn-on-Forecast system. Part I: Radar data experiments. *Wea. Forecasting*, **30**, 1795–1817, https://doi.org/10.1175/WAF-D-15-0043.1.

Whitaker, J. S., T. M. Hamill, X. Wei, Y. Song, and Z. Toth, 2008: Ensemble data assimilation with the NCEP Global Forecast System. *Mon. Wea. Rev.*, **136**, 463–482, https://doi.org/10.1175/2007MWR2018.1.

Wooster, M. J., G. Roberts, G. L. Perry, and Y. J. Kaufman, 2005: Retrieval of biomass combustion rates and totals from fire radiative power observations: FRP derivation and calibration relationships between biomass consumption and fire radiative energy release. *J. Geophys. Res.*, **110**, D24311, https://doi.org/10.1029/2005JD006318.

Yussouf, N., and K. H. Knopfmeier, 2019: Application of Warn-on-Forecast system for flash-flood producing heavy convective rainfall events. *Quart. J. Roy. Meteor. Soc.*, **145**, 2385–2403, https://doi.org/10.1002/qj.3568.

Zhang, J., J. S. Reid, and B. N. Holben, 2005: An analysis of potential cloud artifacts in MODIS over ocean aerosol optical thickness products. *Geophys. Res. Lett.*, **32**, L15803, https://doi.org/10.1029/2005GL023254.

Ziegler, C. L., 1985: Retrieval of thermal and microphysical variables in observed convective storms. Part I: Model development and preliminary testing. *J. Atmos. Sci.*, **42**, 1487–1509, https://doi.org/10.1175/1520-0469(1985)042<1487:ROTAMV>2.0.CO;2.

Zrnić, D., P. Zhang, V. Melnikov, and D. Mirkovic, 2020: Of fire and smoke plumes, polarimetric radar characteristics. *Atmosphere*, **11**, 363, https://doi.org/10.3390/atmos11040363.